A protein hydroxylase couples epithelial membrane biology to nucleolar ribosome biogenesis

Eline Hendrix[1,2#], Regina Andrijes[1,3#], Uncaar Boora[1], Arashpreet Kaur[1], James R Bundred[1,4], Adam Zayer[5,6], Raphael Heilig[7], Christian A E Westrip[1], Sally C Fletcher[1], Charlotte D Eaton[1,8], Tristan J Kennedy[1], Sonia Piasecka[1], Roman Fischer[7], Stephen J Smerdon[1], Mathew L Coleman[1§]

[1]Institute of Cancer and Genomic Sciences, University of Birmingham, Birmingham, UK
[2]Present address: Department of Biochemistry, Stanford University, Stanford, California, USA
[3]Present address: GSK, Gunnels Wood Rd, Stevenage, UK
[4]Present address: School of Medicine, University of Leeds, Woodhouse, Leeds, UK
[5]Centre for Cellular and Molecular Physiology, University of Oxford, Headington, Oxford, UK
[6]Thermo Fisher Scientific, Cambridge, UK
[7]Target Discovery Institute, Nuffield Department of Medicine, NDM Research Building, University of Oxford, Old Road Campus, Roosevelt Drive, Headington, Oxford, UK
[8]Present address: School of Medicine, UCSF, San Francisco, USA
[§]To whom correspondence should be addressed: *m.coleman@bham.ac.uk*
[#]These authors contributed equally

Abstract

Jumonji-C (JmjC) ribosomal protein hydroxylases are an ancient class of oxygen- and Fe(II)-dependent oxygenases that spawned the wider JmjC family and Histone Lysine Demethylases (KDMs) in eukaryotes. Myc-induced Antigen (MINA) has been implicated in ribosome biogenesis and was assigned as a nucleolar-localized JmjC histidyl hydroxylase of the large ribosomal subunit protein RPL27A, consistent with reports that it supports cell growth and viability in a variety of tumor cell types. Reported roles in diverse aspects of disease biology may be consistent with additional MINA functions, although the molecular mechanisms involved remain unclear. Here, we describe an extra-nucleolar interaction of MINA with the Hinge domain of the membrane-associated guanylate kinase, MPP6. We show that MINA promotes the expression and membrane localization of MPP6 and that the MINA-MPP6 pathway is required for epithelial tight junction integrity and barrier function. The function of MINA in this novel pathway is suppressed by ribosomal RNA transcription and the nucleolar MINA interactome, which sequesters MINA in the nucleoli of growing cells. Our work sheds light on how quiescent cells lose adhesion as they switch to proliferate states associated with increased ribosome biogenesis.

Keywords: Myc, ribosome biogenesis, tight junction, polarity, barrier function, RNA polymerase I, protein hydroxylase, MAGUK, polarity

Introduction

Cross-talk between cellular processes is key to enabling a coordinated multisystem response to a change in cell fate. The switch to a proliferative state requires increased metabolic activity and accumulation of biomass to feed cell growth and cell cycle-dependent changes in adhesion to support division (Jones et al., 2019; Pelletier et al., 2018; Zhu and Thompson, 2019). Cells have evolved sophisticated signaling mechanisms to couple such processes. For example, bidirectional cross-talk has been demonstrated between cell adhesion and the cell cycle (Jones et al., 2019). Whether cell adhesion is coupled to other fundamental processes linked to growth remains unclear.

Ribosomal RNA (rRNA) synthesis is a rate-limiting step of ribosome biogenesis and is upregulated as cells switch from growth-arrested to proliferative states in response to major growth responsive signaling pathways and transcription factors, such as Myc (Pelletier et al., 2018; van Riggelen et al., 2010). Activation of Myc or the RNA polymerase I (RNApol1) transcription initiation factor RRN3 is sufficient to induce RNApol1 activity and proliferation in human epithelial cells (Arabi et al., 2005; Grandori et al., 2005; Rossetti et al., 2010; Rossetti et al., 2016). Remarkably, normal 3D morphogenesis (which requires functional polarity and adhesion) is impaired under such conditions (Rossetti et al., 2010; Rossetti et al., 2016), suggesting that ribosome biogenesis, like the cell cycle, might also be coupled to epithelial membrane biology in some way.

MINA is a nucleolar-localized Myc target gene implicated in ribosome biogenesis (Bundred et al., 2018; Eilbracht et al., 2005; Tsuneoka et al., 2002). It is a member of the 2-oxoglutarate (2OG)-, Fe(II)-, and oxygen-dependent oxygenase family, and is highly related to NO66, a prokaryotic orthologue of which is believed to have evolved into the eukaryotic JmjC enzymes, including KDMs (Chowdhury et al., 2014). Despite the presence of a JmjC catalytic domain, detailed structural and biochemical studies suggest that MINA and NO66 may not be KDMs (Chowdhury et al., 2014). Indeed, they catalyze non-redundant and site-specific histidine hydroxylation of the large ribosomal subunit proteins RPL27A and RPL8, respectively (Ge et al., 2012). Hydroxylation has been proposed to support the optimal conformation of the target residue to promote its interaction with rRNA (Yanshina et al., 2020). Consistent with a positive role in ribosome biogenesis/function, multiple studies have described upregulation of MINA in rapidly growing cells, including in tumors (reviewed in (Bundred et al., 2018)). However, recent reports have also implicated MINA in suppressing cell migration, invasion, and epithelial-to-mesenchymal transition (EMT) (Komiya et al., 2010; Yu et al., 2014). How MINA controls these aspects of epithelial biology, and whether it is independent of, or may be coupled to, its role in nucleolar ribosome biogenesis, remains unclear.

Here, we describe a novel extra-nucleolar function for MINA in epithelial barrier function through its pseudosubstrate-like interaction with MPP6, a member of the 'palmitoylated membrane protein' (MPP) subfamily of the MAGUK superfamily of cell adhesion and polarity adaptor proteins. Furthermore, we provide evidence suggesting that increased RNAPol1 activity sinks MINA into the nucleolus to suppress the role of MINA in cell adhesion, thereby coupling ribosome biogenesis to epithelial membrane biology.

Results

MINA promotes epithelial barrier function

Although MINA has been implicated as an oncogenic driver of tumor proliferation, there is emerging literature on its role in suppressing cell migration and invasion. However, these functional studies have generally focused on the role of MINA in highly proliferative cells that have undergone a robust EMT, such as rapidly proliferating tumor cell lines (Bundred et al., 2018) and references therein)). MINA is ubiquitously expressed in normal healthy human tissues (Figure S1), and yet its role in such contexts is poorly characterized. To begin to explore its physiological role in more detail we studied MINA in intestinal epithelial cells that retain good cell adhesion, polarity, and barrier function, and that can differentiate and undergo morphogenesis in 3D (Jaffe et al., 2008; Sambuy et al., 2005). As such, we generated Caco-2 cell lines stably expressing doxycycline-inducible MINA shRNA sequences. In these cells MINA depletion did not affect proliferation (Figure S2) or grossly alter apico-basal asymmetry, as assessed by the localization of tight and adherens junction markers ZO-1 and E-cadherin, respectively (Figure 1A). However, we observed an increase in cell perimeter and cell flattening following MINA knockdown (Figures 1A and 1B). MINA depletion also resulted in delayed formation of transepithelial electrical resistance (TEER; Figure 1C) and a reduction in 'domes' (Figures 1D and 1E), which are normally formed when fluid is pumped under a cell monolayer, in the context of good cell:cell adhesion. Taken together, these data suggest that MINA may be required for tight junction (TJ) integrity and barrier function (MacCallum et al., 2005; Srinivasan et al., 2015). Consistent with this hypothesis, we noted reduced membrane localization and expression of tight junction-associated protein Claudin-1 in response to MINA depletion (Figures 1F, 1G and 1H). How a nucleolar ribosomal protein hydroxylase regulates such membrane-related biology is unclear.

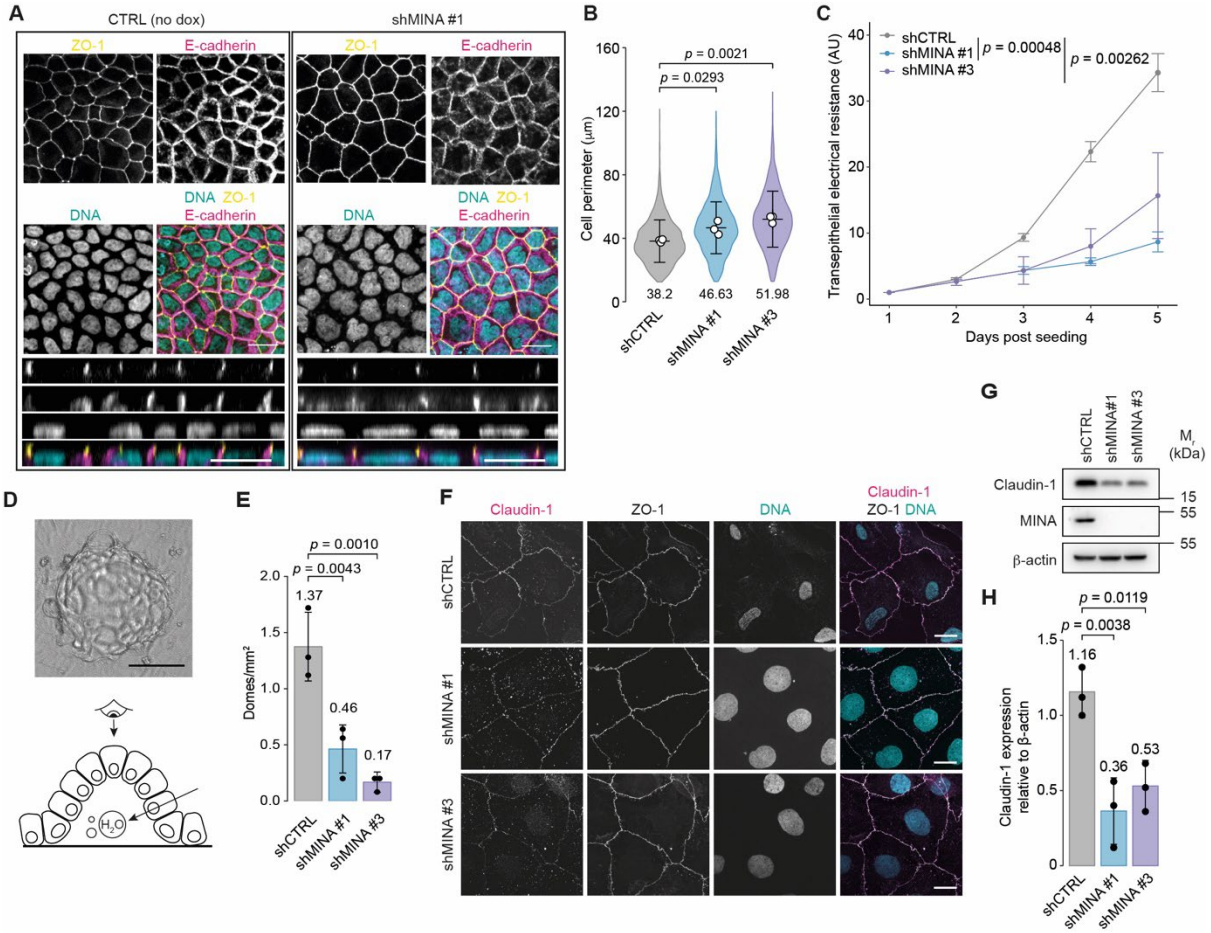

Figure 1. MINA promotes tight junction integrity and epithelial barrier function

(A) *Increased perimeter of cells in MINA-depleted monolayers. Caco-2 cells expressing a non-targeting (shCTRL) or MINA-targeting shRNA (shMINA#1) were grown on a semi-permeable membrane for 10 days and stained for ZO-1 (yellow), E-cadherin (magenta) and DNA (DAPI, cyan). Consecutive images were taken from the basal to the apical side and presented as a maximum projection image (top panels) or orthogonal view (rectangular bottom panels). Orthogonal views show the basal side at the bottom and apical side (as indicated by ZO-1) at the top. Scale bars, 20 µm.*

(B) *Quantification of cell perimeters under conditions presented in (A). Violin plot represents the data from 3 independent experiments. n = 4572 (shCTRL), 2616 (shMINA #1) and 2426 (shMINA #3) cells. The average of each condition is shown underneath each respective violin.*

(C) *Delayed establishment of transepithelial electrical resistance (TEER) in MINA-depleted cells. Monolayer integrity and permeability were analyzed on the indicated days by measuring the electrical resistance across the monolayer. Line graph shows the average of three technical repeats of one representative biological experiment. The experiment was repeated 5 times with similar results.*

(D) *Top, phase-contrast image of a dome, as viewed from the top. Scale bar, 100 µm. Bottom, illustration of a dome, as viewed from the side.*

(E) *Quantification of dome formation in monolayers of stable Caco-2 cells expressing the indicated shRNA sequences. Bars represent the average number of domes per mm^2 of n = 3 independent experiments. The average of each condition is shown above each respective bar.*

(F) *Altered localization of tight junction protein Claudin-1 following MINA knockdown.*

Representative images of Caco-2 monolayers expressing the indicated shRNAs were stained for Claudin (magenta), ZO-1 (gray) and DNA (DAPI; cyan). Scale bars, 20 µm.
(G) *Reduced Claudin-1 protein expression in response to MINA knockdown. Extracts from Caco-2 cells expressing the indicated shRNA sequences were grown into a monolayer over 5 days and immunoblotted for Claudin-1 (23 kDa) and MINA (53 kDa). β-actin was used as loading control. Uncropped images are shown in source data.*
(H) *Quantification of (G). Bar graph shows Claudin-1 expression relative to β-actin. Bars represent the average of n = 3 biological repeats.*
(B), (C), (E), and (H); Statistical significance was determined using a one-way analysis of variance (ANOVA) and p values were calculated post-hoc using a Dunnett's test for multiple comparisons. Error bars, standard deviation (SD).

MINA localization is dependent on its nucleolar interactome and active ribosome biogenesis

To investigate the role of MINA in epithelial membrane biology we first re-evaluated its subcellular localization. Consistent with reports describing nucleolar MINA staining in highly proliferative normal tissues, such as the testes (Tsuneoka et al., 2006), and in tumors (reviewed in (Bundred et al., 2018)), we observed strong nucleolar enrichment of MINA in rapidly growing mesenchymal-like cell lines (e.g. SW620 and A549; Figure 2A). Surprisingly, this enrichment was diminished in slower growing cell lines with a more epithelial morphology. In U2OS and Caco-2 cells the localization of MINA appeared heterogenous with some cells showing diffuse nucleoplasmic staining and no nucleolar enrichment (Figures 2A and S3A).

We hypothesized that the subcellular localization of MINA might be related to growth status. To test this, we cultured Caco-2 to either subconfluence or confluence (Figure 2B): In subconfluent cells we observed a more homogenous subcellular distribution of MINA with diffuse nucleoplasmic staining *and* nucleolar enrichment. In confluent cells MINA distributed evenly throughout the nucleus without any nucleolar enrichment. The nucleolar enrichment of overexpressed MINA was partly dependent on its catalytic activity in subconfluent cells, suggesting a role for RPL27A hydroxylation (Figures 2C and S3B). To explore whether MINA localization is dynamic and responds to external cues we grew Caco-2 cells to confluence before scratching the monolayer. As expected, confluent cells distal to the scratch showed nucleoplasmic MINA localization. However, cells proximal to the scratch showed elevated levels of MINA and nucleolar enrichment (Figure 2D). Taken together, these data suggest that the growth status of the cell is an important determinant of MINA localization.

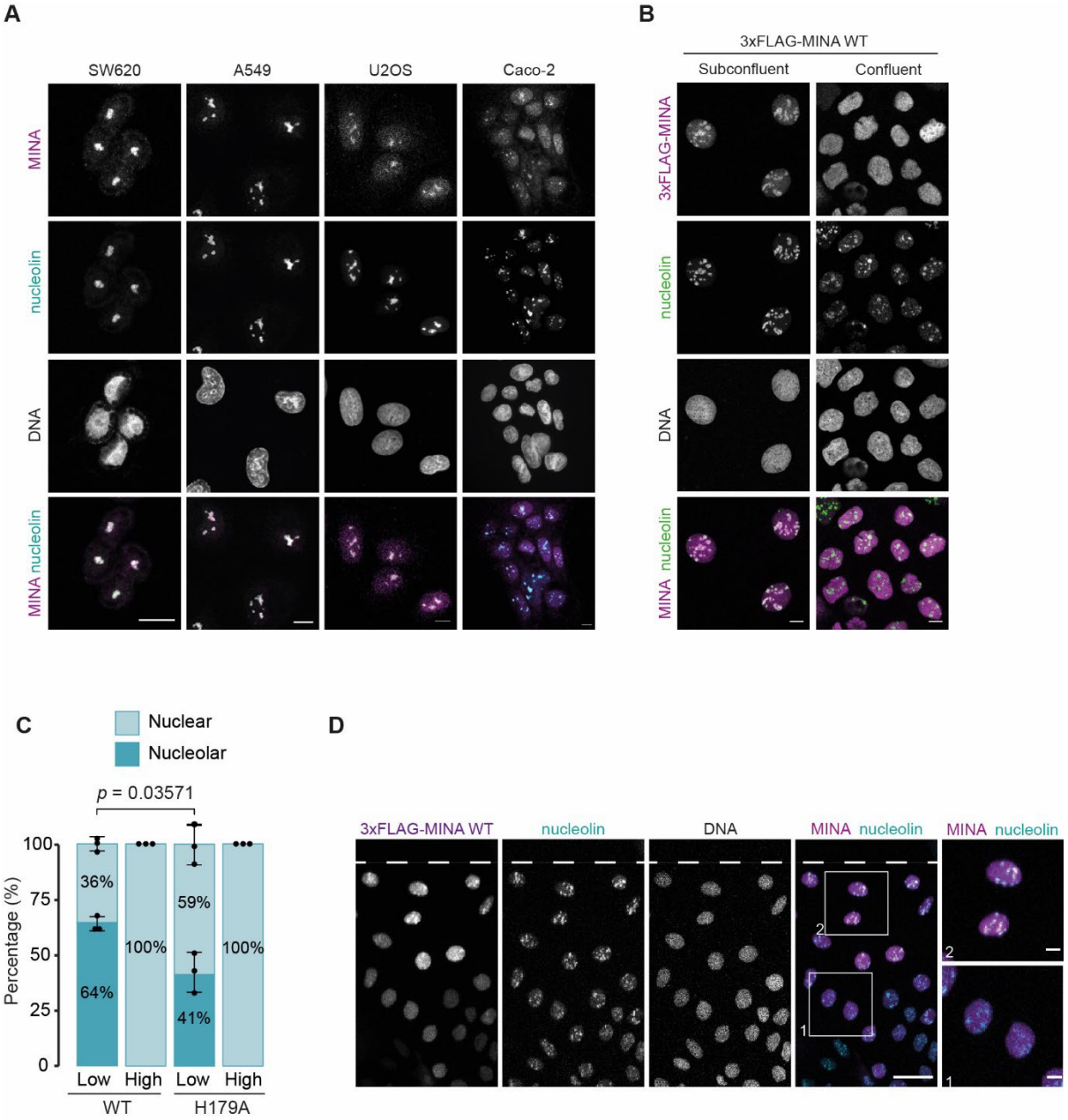

Figure 2. MINA nucleolar localization is regulated by growth and hydroxylase activity

(A) *Localization of MINA in selected cancer cell lines. Representative immunofluorescence images showing nucleolar and/or nucleoplasmic MINA. Cells were fixed with methanol and stained for endogenous MINA (magenta) and the nucleolar marker nucleolin (cyan). Scale bars, 10 µm.*

(B) *Nucleolar MINA localization depends on cell confluence. Representative immunofluorescence images showing the localization of wildtype (WT) 3xFLAG-MINA in subconfluent and confluent conditions. Cells were incubated with 0.1 µg/mL doxycycline for 48 h to induce expression of 3xFLAG-MINA and stained with an antibody raised against endogenous MINA (magenta). To confirm that the detected signal was of overexpressed, exogenous 3xFLAG-MINA, an empty vector control was used (Figure S3B). Cells were counterstained for nucleolin (NCL, green) and DNA (DAPI, gray). Scale bars, 10 µm*

(C) *Bar graph showing the percentage of cell in which nucleolar enrichment could ('Nucleolar') or could not ('Nuclear') be observed. 'Low' and 'High' refer to the level of confluence. Bars*

181 *show the average of three biological repeats. Error bars, SD. A total of one hundred cells were*
182 *counted per condition per experiment. Samples were blinded before analysis. Statistical*
183 *significance was determined using an unpaired t-test.*
184 ***(D)** MINA becomes enriched in the nucleolus following disruption of a confluent monolayer. A*
185 *scratch was introduced to disrupt a confluent monolayer of Caco-2 cells expressing wildtype*
186 *3xFLAG-MINA. Cells were fixed 24 h after the scratch was made. Re-localization of 3xFLAG-*
187 *MINA was observed in cells proximal to the scratch (top, indicated by the white dashed line).*
188 *In contrast, at a distance from the scratch, 3xFLAG-MINA remained in the nucleoplasm*
189 *(bottom). Scale bars, 50 or 10 (enlargements) µm.*
190

191 Considering the importance of MINA hydroxylase activity, and the established links between
192 growth and ribosome biogenesis, we hypothesized that increased ribosome biogenesis might
193 act as a nucleolar sink for MINA. Consistent with this possibility, we observed significant
194 nucleolar enrichment of nascent proteins that colocalized with MINA in subconfluent cells
195 (Figure 3A). Under these conditions, inhibition of rRNA transcription and ribosome biogenesis
196 with RNAPol1 inhibitors was sufficient to redistribute MINA from the nucleolus to the
197 nucleoplasm (Figures 3B and S4A) (Eilbracht et al., 2005). Publicly available SILAC proteomic
198 data demonstrate that the response to RNAPol1 inhibition is rapid and dynamic (Figure 3C)
199 (Andersen et al., 2005). Conversely, overexpression of the RNAPol1 activator RRN3 was
200 sufficient to enrich some MINA in the nucleoli of confluent cells (Figure S4B). Nucleophosmin
201 (NPM1) is a highly abundant nucleolar protein involved in ribosome biogenesis and a major
202 MINA-binding partner (Eilbracht et al., 2005; Ge et al., 2012). To test whether NPM1
203 contributes to nucleolar sequestration of MINA we targeted it with siRNA in subconfluent Caco-
204 2 cells. Consistent with the hypothesis, loss of NPM1 expression was sufficient to redistribute
205 MINA to the nucleoplasm (Figure S4C). Overall, our localization analyses suggest that
206 nucleolar enrichment of MINA is dependent on elevated levels of ribosome biogenesis and its
207 nucleolar interactome. In cells where these determinants are lost or suppressed, MINA is
208 redistributed to the nucleoplasm, where (we hypothesize) it undertakes an alternative function
209 in epithelial membrane biology.

210 We reasoned that a nucleolar localization mutant would support efforts to dissect nucleolar
211 versus extra-nucleolar MINA functions. We searched the MINA primary sequence for
212 nucleolar localization sequences (NoLSs) (Scott et al., 2011) and identified two potential
213 candidates, one at the N-terminus and a bipartite-like motif within residues 100-125 (Figure
214 S5A). The latter was more highly conserved than the N-terminal sequence (Figure S5B). The
215 basic residues at the C-terminal end of the conserved bipartite motif (R125/K126) are within
216 an a-helix and their side chains are solvent-exposed, which are known determinants of NoLSs
217 (Figure 3D) (Scott et al., 2010). The C-terminal part of bipartite NoLSs have previously been
218 shown to be involved in nucleolar targeting (Scott et al., 2010). Therefore, we considered

R125/K126 as residues of interest to experimentally test their contribution to MINA nucleolar localization. Consistent with predictions, an R125G/K126G mutant (NoLS) was unable to localize to the nucleolus (Figure 3E) and did not interact with the nucleolar targets RPL27A and NPM1 (Figure 3F). The R125G/K126G mutation retained nuclear localization (Figure 3E) and hydroxylase activity (Figure S5C), suggesting that MINA NoLS mutant is a viable tool for investigating the extra-nucleolar role of MINA.

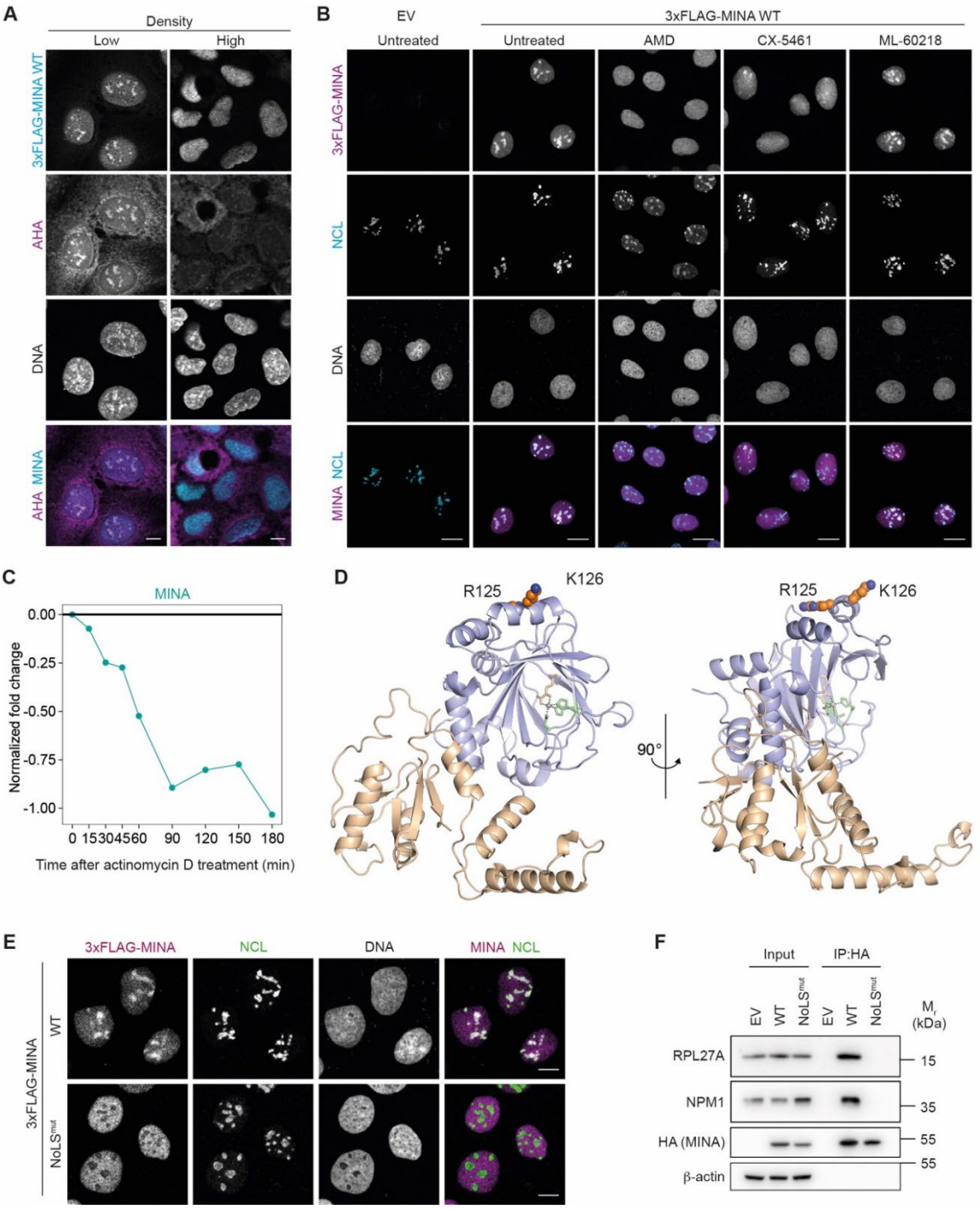

Figure 3. Determinants of subnuclear MINA localization

(A) *3xFLAG-MINA colocalizes with newly synthesized proteins in the nucleoli of subconfluent cells. Stable Caco-2 cells expressing wildtype (WT) 3xFLAG-MINA and seeded at a high or*

229 *low density were treated with methionine analogue L-Azidohomoalanine (AHA, magenta) for*
230 *1 h before the cells were fixed and labelled using Click-IT chemistry. Cells were co-stained*
231 *for MINA (cyan). Scale bars, 10 µm.*
232 ***(B)** Nucleoplasmic translocation of MINA in response to RNA polymerase I inhibitors.*
233 *Expression of 3xFLAG-MINA was induced in subconfluent Caco-2 cells using 0.1 µg/mL*
234 *doxycycline for 48 h prior to treatment. Empty vector (EV) or WT 3xFLAG-MINA expressing*
235 *cells were either untreated or treated with 40 ng/mL actinomycin D (AMD) or CX-5461 to inhibit*
236 *RNA polymerase I for 4 h. Parallel samples were treated with RNA polymerase III inhibitor*
237 *ML-60218 to determine the specificity of the observed effects. Cells were stained for MINA*
238 *(magenta), nucleolin (NCL, cyan) and DNA (DAPI, gray). Scale bars, 20 µm.*
239 ***(C)** SILAC proteomic data demonstrate that the nucleolar abundance of MINA declines rapidly*
240 *in response to actinomycin D (see Anderson et al, main text ref (Andersen et al., 2005)). The*
241 *authors treated HeLa cells with 1 µg/mL actinomycin D for the indicated times before mass*
242 *spectrometry-based quantification of the nucleolar proteome.*
243 ***(D)** Ribbon representation of a MINA monomer showing residues that contribute to MINA*
244 *nucleolar localization (R125/K126) and the catalytic core in purple. Protein Data Bank (PDB)*
245 *ID = 4BXF. Structures were visualized using PyMOL.*
246 ***(E)** R125G/K126G mutations prevent MINA nucleolar localization. Caco-2 cells expressing*
247 *either WT or 3xFLAG-MINA R125G/K126G (NoLS^{mut}) were stained for MINA (magenta),*
248 *nucleolar protein nucleolin (NCL, green) and DNA (DAPI, gray). Scale bars, 10 µm. Expression*
249 *of 3xFLAG-MINA was induced by treatment with 0.1 µg/mL doxycycline for 48 h.*
250 ***(F)** MINA NoLS^{mut} does not interact with nucleolar interactors RPL27A and NPM1. Anti-HA*
251 *immunoprecipitates (IP) from extracts of HEK293T cells transiently expressing the indicated*
252 *HA-MINA constructs were immunoblotted for RPL27A (17 kDa), NPM1 (33 kDa) and HA*
253 *(MINA, 53 kDa). β-actin (42 kDa) was used as loading control. Input = cell extract prior to*
254 *immunoprecipitation (for RPL27A and NPM1 the input is 1% of the IP, for HA and β-actin it is*
255 *50%). β-actin (42 kDa) was used as loading control. Uncropped western blot images are*
256 *presented in source data.*
257

258

259 **Extra-nucleolar MINA interacts with membrane palmitoylated protein 6 (MPP6)**

260 To investigate how extra-nucleolar MINA regulates barrier function we next sought to identify
261 extra-nucleolar MINA interactors. We hypothesized that a physiologically relevant extra-
262 nucleolar MINA interactor might exist in multiple independent cell types and be enriched in
263 NoLS versus wildtype MINA pulldowns. Therefore, we first immunopurified wildtype 3xFLAG-
264 MINA from three diverse cell types (Caco-2, U2OS, and mouse embryonic fibroblasts) before
265 trypsinolysis and MS-based protein identification. We removed contaminants present in
266 control samples before applying strict filtering criteria to identify only the highest confidence
267 and most abundant interactors. Cross-referencing the three datasets identified just four
268 proteins in common, two of which were the known interactors RPL27A and NPM1. Next, we
269 compared NoLS and wildtype MINA proteomic screens performed in Caco-2 cells to identify
270 proteins with increased binding to extranucleolar MINA: We cross-referenced these

271 candidates with the four proteins identified in multiple cell lines above, which identified one
272 protein, MPP6 (Figure 4A). Because MPP6 is a member of the MAGUK superfamily of cell
273 adhesion and polarity proteins (Figure S6) (Chytła et al., 2020), we considered it a viable
274 candidate to mediate the extra-nucleolar functions of MINA in epithelial membrane biology.
275 Therefore, we sought to study the MINA:MPP6 interaction in more detail.

276 First, we independently validated the proteomic results in multiple cell types (Figures 4B, S7A
277 and S7B). As expected, we observed a specific interaction between MPP6 and MINA that was
278 increased in the nucleolar localization mutant. Intriguingly, the interaction was dependent on
279 the catalytic activity of MINA, being completely abolished by an inactivating Fe(II)-binding
280 mutation (H179A) (Figures 4B, S7A and S7B) (the role of MINA activity is investigated in more
281 detail below). Next, we explored the specificity of the MINA:MPP6 interaction. Under
282 conditions where endogenous MPP6 interacted with HA-MINA, it did not bind to the closely
283 related hydroxylase NO66 (Figure S7C). Similarly, FLAG-MINA coprecipitates with MPP6-HA,
284 but not with the highly related MPP2 (sequence identity = 65.2%) (Figure S7D). Endogenous
285 MPP6 coprecipitates endogenous MINA (Figure S7E). Consistent with the MINA localization
286 (Figure 1) and proteomic analyses (Figure 4), immunofluorescence and proximity ligation
287 assays (PLA) indicate that 3xFLAG-MINA and MPP6-HA colocalize and interact in the
288 nucleoplasm of subconfluent cells (Figures 4C and Figure S7F). Moreover, the PLA signal
289 was reduced in confluent monolayers (Figure 4C), consistent with the translocation of MPP6
290 from the nuclear compartment to the membrane (Figure S7G). Unsurprisingly therefore, less
291 MPP6 interacts with 3xFLAG-MINA in highly confluent monolayers of Caco-2 (Figure S7H).
292 Increasing the pool of extra-nucleolar MINA in subconfluent cells (through RNApol1 inhibition,
293 Figure 1) increased its interaction with MPP6 (Figure 4D). The NoLS mutant showed
294 constitutively increased MPP6 binding, as expected, and was completely resistant to the
295 effects of RNApol1 inhibition (Figure 4D). These data indicate that RNApol1 activity and
296 ribosome biogenesis sequester MINA in the nucleolus of subconfluent cells, thereby
297 suppressing its interaction with MPP6.

298

299

300

301

302

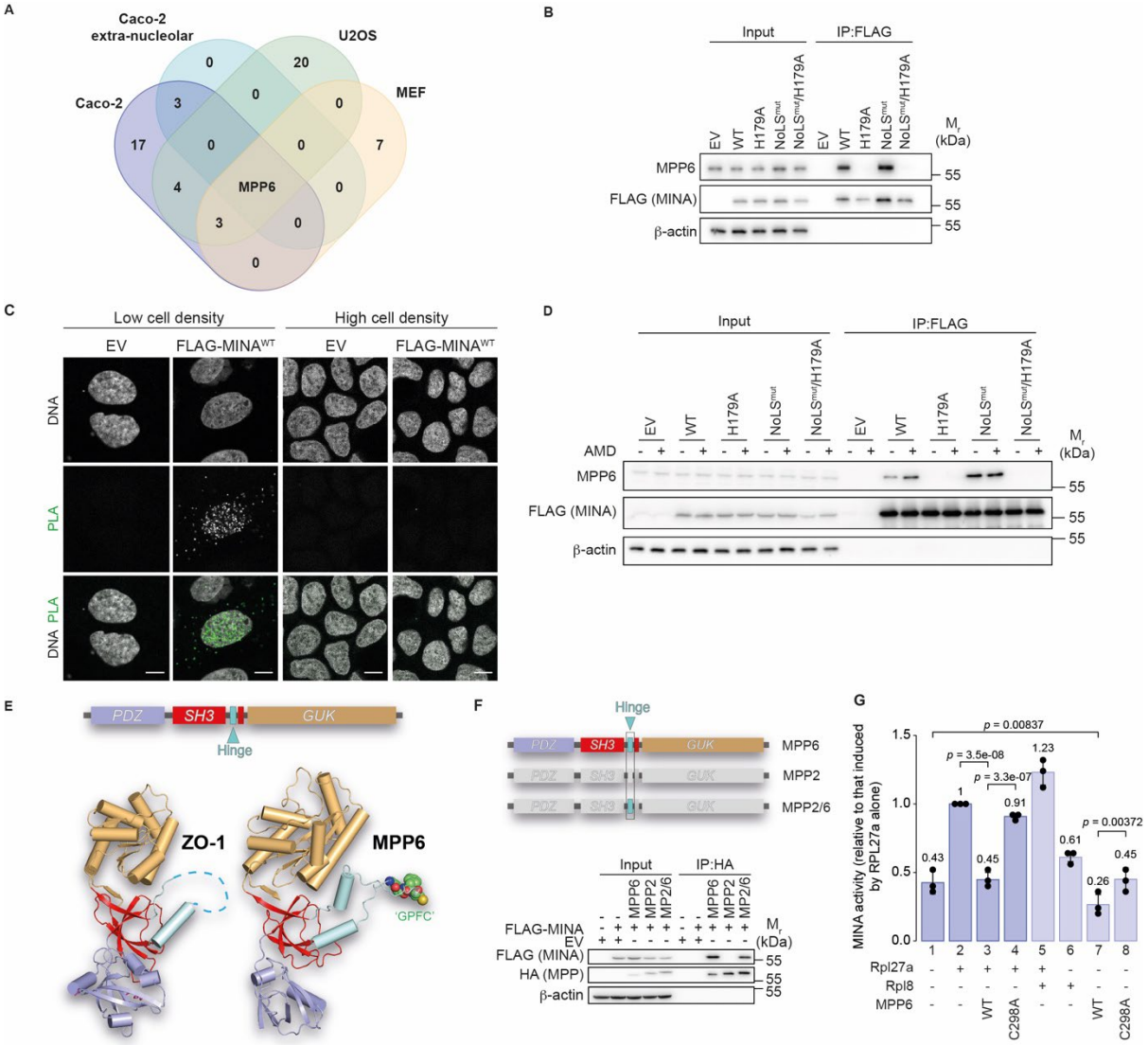

Figure 4. Extra-nucleolar MINA interacts with MPP6, a member of the 'membrane-associated guanylate kinase' (MAGUK) family

(A) *Venn diagram showing the overlap between high stringency MINA-interactomes identified in Caco-2, U2OS and MEF cells. Note that the only common factor that was also upregulated with extra-nucleolar MINA (NoLS^{mut}) was MPP6.*

(B) *Validation of proteomic data. Anti-FLAG immunoprecipitates (IP) from extracts of stable Caco-2 cells expressing the indicated doxycycline-inducible 3xFLAG-MINA constructs were immunoblotted for endogenous MPP6 (61 kDa), FLAG (MINA, 53 kDa). For MPP6 the input is 0.6% of the IP, for FLAG and β-actin it is 31%.*

(C) *Proximity ligation assays (PLA, green foci) indicate that MINA and MPP6 preferentially interact in the nuclei (gray) of subconfluent Caco-2 cells. Scale bars, 10 µm.*

(D) *The interaction of MPP6 with MINA is suppressed by RNA polymerase I activity. Anti-FLAG IPs from extracts of stable SW620 cells expressing an empty vector (EV) or the indicated 3xFLAG-MINA constructs were immunoblotted for MPP6 (61 kDa) and FLAG (MINA, 53 kDa). Expression of 3xFLAG-MINA was induced with 0.2 µg/mL doxycycline for 24 h before the cells were treated with 40 ng/mL actinomycin D (AMD) for 4 h. Input = 1%.*

(E) *MPP6 domain architecture. Top, Cartoon representation of the 'PSG' supramodule. Bottom, Comparison of the X-ray structure of the PDZ-SH3-GUK region from a canonical*

322 *MAGUK protein ZO-1 (PDBID:3SHW) and the predicted structure of the equivalent region of*
323 *MPP6 generated with AlphaFold. The GPFCG motif is highlighted in space-filling*
324 *representation and is located at the tip of the unstructured 'Hinge' insert. The yellow ball*
325 *represents residue C298.*
326 ***(F)** The Hinge domain of MPP6 is sufficient for MINA binding. An MPP2 chimera that contains*
327 *the Hinge domain of MPP6 (AAs 285-338) ('MPP2/6'), but not wildtype MPP2, coprecipitates*
328 *FLAG-MINA. Top, Graphical representation of the constructs used in the bottom panel.*
329 *Bottom, Anti-HA immunoprecipitates from extracts of HEK293T cells expressing the indicated*
330 *constructs were immunoblotted as indicated. For FLAG and β-actin the input is 10% of the IP,*
331 *for HA it is 20%.*
332 ***(G)** An MPP6 peptide containing the minimal determinants for MINA binding*
333 *(SQFLEEKRKAFVRRDWDNS**GPFCG**TISSKKKKK) blocks RPL27A peptide*
334 *(GRGNAGGL**H**HHRINFDKYHP)-induced MINA activity in vitro. An NO66 substrate peptide*
335 *(Rpl8; NPVEHPFGGGNHQHIGKPSTI), which is known not to support MINA activity (Ge et*
336 *al., 2012) was used as negative control. MINA activity was determined using an indirect*
337 *coupled assay based on succinate production (see Methods). Bars represent the average of*
338 *n = 3 biological repeats. Averages are indicated above each respective bar. Error bars, SD.*
339 *Statistical significance was determined using a one-way ANOVA and p values were calculated*
340 *post-hoc using a pairwise t test. P values were adjusted using the Benjamini-Hochberg*
341 *correction for multiple comparisons. Uncropped western blot images are presented in source*
342 *data.*
343

344

345 **The Hinge regions of MPP2 and MPP6 confer MINA binding specificity**

346 As scaffold proteins, MAGUK proteins are characterized by the presence of several protein-
347 protein interaction domains. These include a characteristic PDS-95/DLG/ZO-1 (PDZ) – Src
348 homology 3 (SH3) – guanylate kinase (GUK) tandem motif ('PSG') (Figure S6) that can fold
349 into a structural supramodule (Ye et al., 2018). Folding requires a disordered 'Hinge' region
350 that loops out of the non-canonical SH3 domain and that includes a polybasic sequence
351 implicated in membrane localization and protein:protein interactions (Hanada et al., 2003).
352 Modeling the tertiary structure of MPP6 using AlphaFold confirms the likelihood that the PDZ,
353 SH3, and GUK domains of MPP6 form a PSG supramodule analogous to ZO-1 (Figure 4E).
354 Furthermore, the AlphaFold model of MPP6 also predicts the presence of a Hinge insert within
355 its non-canonical split SH3 domain.
356
357 To test the requirements of these MPP6 domains for MINA binding we analyzed a series of
358 MPP6 truncation mutants in immunoprecipitation and immunofluorescence experiments
359 (Figures S8A, S8B, and S8C). The results suggest that the minimal MPP6 domain required
360 for MINA binding is within the non-canonical SH3 domain, i.e. amino acids 285-338, which
361 contains the so-called Hinge domain (Figures 4E and S8B). To test whether this domain is
362 sufficient for MINA binding we created an MPP2/6 chimera by swapping the Hinge domain of

363 MPP2 (which does not bind MINA; Figure S7D) with the corresponding domain of MPP6
364 (Figure 4F, top). Immunoprecipitation analysis confirmed that the MPP6 Hinge domain is
365 sufficient for MINA binding in this context (Figure 4F, bottom). To further narrow down the
366 binding determinants, we next focused on the differences in primary sequence between MPP2
367 and MPP6 in this region. The sequence identity of this region is 67.9%, suggesting that the
368 strikingly different MINA binding profiles are determined by the relatively few regions of low
369 homology (Figure S8D). To test the importance of these regions we swapped residues within
370 them in the context of the MPP2/6 chimera. A small insertion at the N-terminal end of the
371 MPP2 Hinge domain was sufficient to prevent MINA binding (Figure S8E). Next, we alanine
372 scanned residues 287-303 within the Hinge domain of full-length MPP6 and identified residues
373 295-299 (sequence GPFCG) as critically required for MINA binding (Figure S8F). These
374 residues are situated at the predicted apex of the unstructured and solvent-exposed loop of
375 the Hinge domain (Figure 4E), and are therefore likely to be available for protein:protein
376 interactions. Together, these data are consistent with a site-specific interaction of MINA with
377 a minimal sequence motif within the Hinge domain of MPP6.
378
379 **The Hinge region of MPP6 mediates a pseudo-substrate-like interaction with MINA**
380 MINA interacts with MPP6 in an activity-dependent manner (Figures 4B, 4D, S7A and S7B).
381 The interaction of MINA with the MPP6 Hinge domain retains its dependence on MINA
382 hydroxylase activity (Figures S8G and S8H). Activity-dependence of binding can be an
383 indicator that a hydroxylase interactor is a novel substrate (Feng et al., 2014; Markolovic et
384 al., 2018). Therefore, we next explored whether MPP6 is hydroxylated by MINA.
385
386 MPP6-3xFLAG was overexpressed in the presence or absence of HA-MINA before
387 immunoprecipitation (Figure S9A), in-solution chymotrypsin digest, and LC-MS/MS analysis.
388 Near complete (98%) peptide-level sequence coverage of MPP6 was achieved in database
389 searches that also considered a wide-range of residue-specific oxidations (Figure S9B).
390 Consistent with the lack of homology between the known substrate RPL27A and the Hinge
391 domain of MPP6 (Figure S9C) we did not detect histidyl hydroxylation in this region. Oxidized
392 peptides encompassing the Hinge domain were detected that could be confidently assigned
393 to W291 (Figures S9D and S9E). However, the stoichiometry was low and did not respond to
394 MINA overexpression (Figure S9F). Neither subconfluent culture (where MINA binding is
395 predicted to increase), or proteasomal inhibition, led to elevated W291 oxidation, even in the
396 presence of MINA overexpression (Figure S9F). We note that tryptophan can undergo
397 spontaneous chemical oxidation as an artefact of sample preparation for MS (Cockman et al.,
398 2019; Perdivara et al., 2010; Verrastro et al., 2015).

399

400 In order to take an orthogonal approach that avoids the limitations of mass spectrometry
401 analysis and artefactual oxidation we next used a coupled in vitro enzyme assay. Although
402 the currently assigned hydroxylase activity of MINA is restricted to histidyl residues, we noted
403 the absence of a histidine in the minimal domain within MPP6 that is required for MINA binding
404 (residues 295-299). Since some closely related JmjC-hydroxylases can target multiple amino
405 acid types (Cockman et al., 2006; Coleman et al., 2007; Yang et al., 2011a; Yang et al.,
406 2011b), we first explored the potential for wider biochemical specificity of MINA, including the
407 amino acids in this region of MPP6 (Gly, Pro, Phe, and Cys). To do this we used RPL27A
408 peptides with the corresponding amino acid substitutions at the H39 target residue: Unlike the
409 wildtype RPL27A peptide sequence, neither H39G, H39P, H38F or H39C peptides were able
410 to support MINA activity (Figure S10A). Similar data were obtained using H39W-, H39S-,
411 H39N-, H39D-, H39K-, and H39R-substituted peptides. These data indicate that MINA does
412 not have a broad biochemical activity and is unlikely to hydroxylate residues found within the
413 MPP6 minimal binding domain. To explore this directly, we tested three MPP6 peptides of
414 varying length and position that overlap the GPFCG motif and wider Hinge region of MPP6
415 (which is sufficient for activity-dependent MINA binding, Figure 4F) (Figure S10B). Unlike the
416 RPL27A peptide, none of the MPP6 peptides supported MINA activity (Figure S10C).
417

418 Overall, therefore, our cell-based and in vitro studies did not identify a MINA-dependent
419 hydroxylation of MPP6. We cannot rule out the presence of a modification that was below the
420 limits of detection, the catalysis of a previously undescribed oxidative modification, or
421 subsequent processing of an oxidized species. However, it is also possible that, unlike the
422 activity-dependent interactions of related JmjC hydroxylases that led to novel substrate
423 assignments (Feng et al., 2014; Markolovic et al., 2018), the activity-dependent interaction
424 described here is unique. For example, the interaction of MPP6 with MINA may require the
425 integrity and availability of the catalytic pocket, rather than being 'activity-dependent' per se.
426 In line with MPP6 binding directly to the MINA catalytic pocket, an MPP6 peptide containing
427 the GPFCG motif prevented RPL27A-induced MINA activity (Figure 4G; compare 2nd and 3rd
428 bar) and significantly reduced its 'uncoupled' turnover (compare 1st and 7th bar). Both effects
429 were specific as they were not observed with a control peptide (NO66 substrate Rpl8)
430 (compare 2nd, 3rd, and 5th bars, and 1st, 6th and 7th bars). Furthermore, both effects of the MPP6
431 peptide were ablated by the C298A substitution (compare 3rd and 4th bar, and 7th and 8th bar)
432 (Figure 4G), which is sufficient to block binding of MPP6 to MINA (Figure S8F). Overall, our
433 data are consistent with the possibility that the solvent exposed C298 residue of the MPP6
434 Hinge domain binds to the MINA catalytic pocket in a pseudo-substrate-like manner.
435

436 **MINA regulates MPP6 expression and localization**

437 Although we did not identify a modification arising from MINA binding to MPP6, we were
438 intrigued that the function of the interaction might be related to the role of the Hinge domain in
439 other MAGUKs, i.e. membrane localization and protein stability (Hanada et al., 2003; Moreno-
440 García et al., 2010). MINA knockdown caused a reduction in membrane staining and increase
441 in nuclear localization of MPP6 in low-density cultures (Figures 5A and 5B), in parallel with a
442 reduction in MPP6 protein expression (Figure 5C). Consistent with these changes being a
443 direct consequence of the interaction with MINA, a constitutively expressed MPP6 mutant that
444 fails to bind MINA (C298A) was nuclear localized and underexpressed (Figures 5D and 5E).
445 These data suggest that the interaction of MINA with MPP6 in the nucleus (Figures 4C)
446 promotes the subsequent localization of MPP6 to the plasma membrane.

447

448 **MPP6 is required for the timely establishment of cell-cell junctions**

449 Considering the effect of MINA knockdown on barrier function (Figure 1) and MPP6 membrane
450 localization and expression (Figures 5A and 5B), we hypothesized that MPP6 knockdown
451 would phenocopy MINA loss of function. Indeed, shRNA knockdown of MPP6 severely
452 impaired dome formation and TEER (Figures 5F, 5G and 5H) and increased the length of the
453 cell perimeter (Figures 5I), with concomitant reduction in membrane staining and expression
454 of Claudin-1 (Figures 5J, S11A and S11B). Similar to MINA knockdown, this occurred in the
455 absence of gross changes in cell proliferation (Figure S11C). To explore the effect of the MPP6
456 C298A mutant we switched to a tunable doxycycline-inducible system, due to the known
457 confounding effects of overexpressing membrane/polarity proteins in some circumstances,
458 and the differential expression of constitutively expressed wildtype and C298A MPP6 (Figure
459 5E). Using this system, we observed that modest expression of MPP6-3xFLAG was sufficient
460 to promote dome formation (Figures 5K and 5L). The MPP6 C298A mutant, which impairs
461 MINA binding, was completely inactive in this regard (Figure 5K and 5L).

462

463

464

465

466

467

468

469

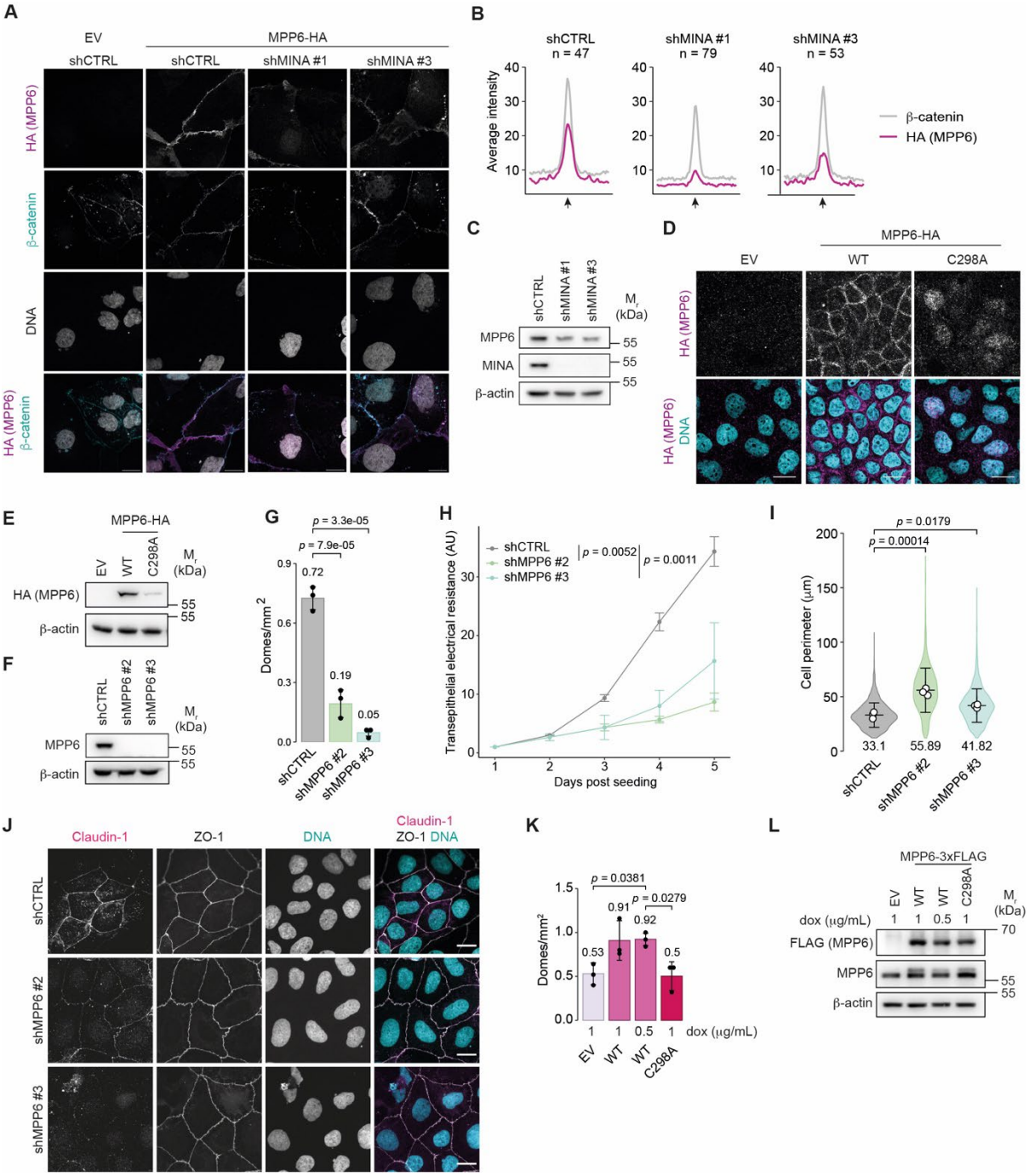

Figure 5. MPP6 promotes tight junction integrity and epithelial barrier function

(A) *MINA depletion reduces membrane localization and increases nuclear distribution of MPP6. Representative immunofluorescence images of subconfluent Caco-2 cells expressing the indicated shRNAs and stained for HA (magenta), β-catenin (cyan) to mark the membranes and DNA (DAPI, gray). Scale bars, 20 μm.*

(B) *Reduced membrane staining of MPP6-HA in MINA-depleted cells under conditions presented in (A). Line graphs indicate the average fluorescence intensity of a line drawn across the membrane connecting two cells, measured with Fiji. The average of n = 3 biological experiments is shown. The total number of images analyzed for each condition is shown above each respective graph. β-catenin was used as membrane marker.*

482 ***(C)*** *MINA depletion reduced MPP6 expression in subconfluent Caco-2 cultures. Whole cell*
483 *extracts from cells expressing the indicated shRNAs were immunoblotted for MPP6 (61 kDa)*
484 *and MINA (53 kDa).*
485 ***(D)*** *Altered localization of HA-tagged MINA-binding mutant MPP6^{C298A}. Stable Caco-2 cell*
486 *lines constitutively expressing an empty vector (EV), wildtype (WT) or MPP6-HA C298A were*
487 *stained for HA (MPP6, cyan) and DNA (DAPI, cyan). Scale bars, 20 µm.*
488 ***(E)*** *Reduced expression of HA-tagged MINA-binding mutant MPP6^{C298A}. Whole cell extracts*
489 *were immunoblotted for HA (MPP6, 61 kDa).*
490 ***(F)*** *Representative immunoblot from whole cell extracts of stable Caco-2 cells expressing the*
491 *indicated shRNAs showing efficient depletion of MPP6 (61 kDa).*
492 ***(G)*** *MPP6 depletion reduces dome formation. Bar graph showing the average number of*
493 *domes per mm^2 of n = 3 independent experiments. The average of each condition is shown*
494 *above each respective bar.*
495 ***(H)*** *Delayed establishment of transepithelial electrical resistance in MPP6-depleted cells. Line*
496 *graph depicts the average of three technical repeats of one biological repeat. The experiment*
497 *was repeated 4 times with similar results. Statistical significance was determined on day 5.*
498 ***(I)*** *Increased perimeter of cells in MPP6-depleted monolayers. Violin plot represents the data*
499 *from n = 3 experiments. Average of each condition is shown underneath each respective violin.*
500 *n = 2612 (shCTRL), n = 1450 (shMPP6 #2) and n = 1958 (shMPP6 #3) cells were quantified.*
501 ***(J)*** *Altered localization of Claudin-1 following MPP6 knockdown. Representative images of*
502 *Caco-2 monolayers expressing the indicated shRNAs were stained for Claudin-1 (magenta),*
503 *ZO-1 (gray) and DNA (DAPI; cyan). Scale bars, 20 µm.*
504 ***(K)*** *MPP6-induced dome formation is dependent on C298. Expression of wildtype (WT) or*
505 *MINA-binding mutant C298A MPP6-3xFLAG were induced with doxycycline (dox) at the*
506 *indicated concentrations. Note that a reduced concentration of dox (0.5 µg/mL) was included*
507 *for WT to allow fair comparison to the reduced expression levels observed for C298A (as also*
508 *presented in (E)). Domes were counted 4 days post seeding.*
509 ***(L)*** *Cell extracts of samples treated as in (K) were immunoblotted for FLAG (MPP6) and MPP6*
510 *(61 kDa).*
511 *(G-I and K) Statistical significance was determined using a one-way ANOVA and p values*
512 *were calculated post-hoc using a Dunnett's multiple comparisons test. Error bars, SD.*
513 *(C, E, F and L) β-actin (42 kDa) was used as loading control. Uncropped western blot images*
514 *are presented in source data.*
515

516 **The MINA-MPP6 pathway is required for normal 3D growth and morphogenesis**

517 To investigate the importance of the MINA-MPP6 pathway in 3D growth and tissue
518 morphogenesis, Caco-2 cells expressing doxycycline-induced control, MINA or MPP6 shRNA
519 were seeded as single cells in Matrigel and grown for 7 days to form polarized spheroids with
520 a fluid-filled lumen (Jaffe et al., 2008). Depletion of MINA or MPP6 was sufficient to interfere
521 with spheroid morphology including lumenogenesis (Figures 6A,B and S12A,B), size (Figure
522 6C,D), and growth (Figure 6E,F). Immunofluorescence analysis revealed a diffuse staining
523 pattern of Claudin-1 and ZO-1 and altered nuclear morphology (Figure 6G,H). Although these
524 observations may be consistent with some level of defective polarity, a luminal surface was
525 still largely maintained in these spheroids (Figure 6G,H). Consistent with the 2D data

presented above, MINA and MPP6 depletion also reduced Claudin-1 levels (Figure S12C,D). Expression of the MINA binding defective MPP6 mutant (C298A) phenocopied MINA and MPP6 loss of function, causing reduced lumenogenesis, decreased spheroid size, and diffuse localization of ZO-1 (Figure 6I).

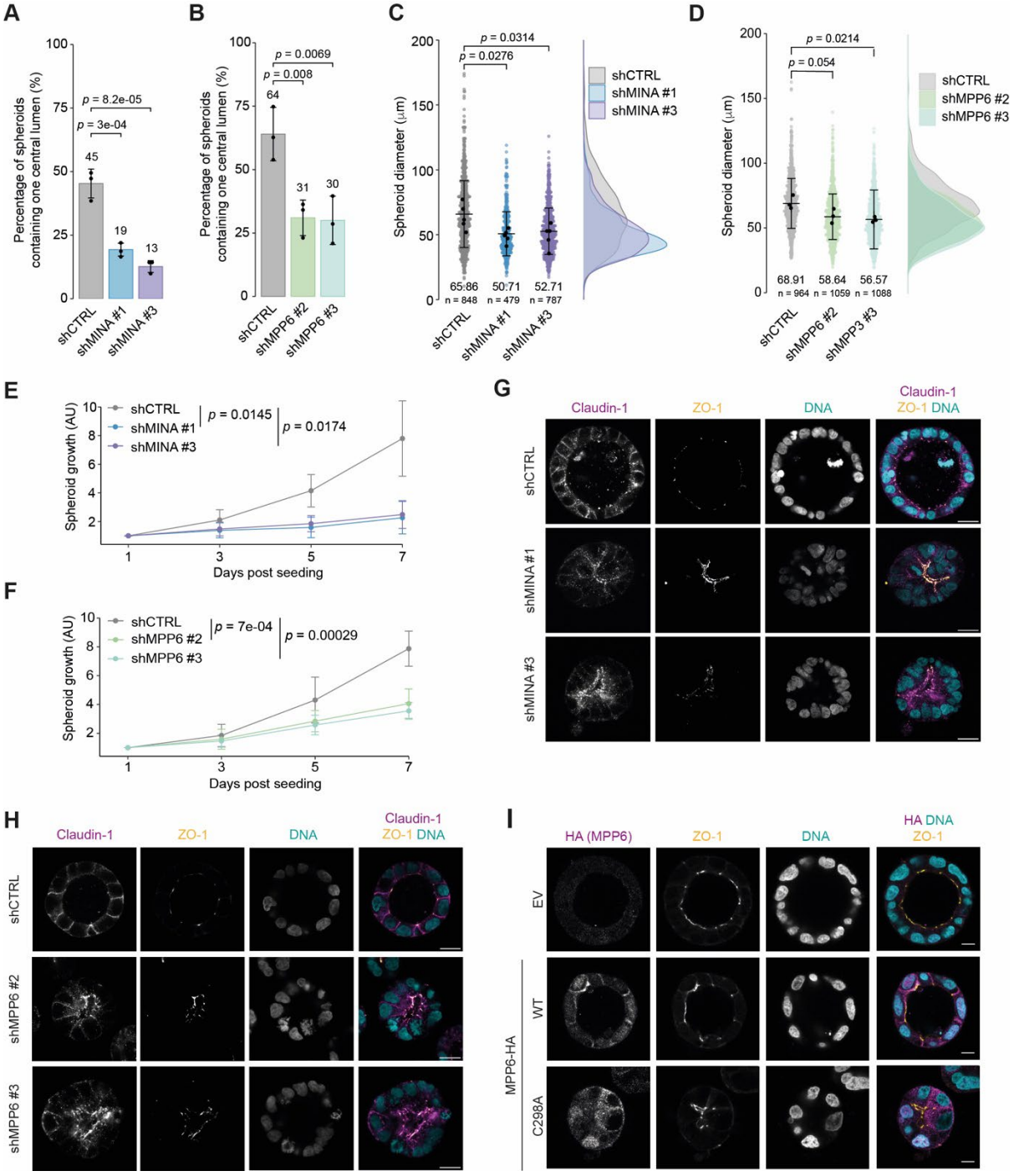

Figure 6. The MINA-MPP6 pathway is required for spheroid lumenogenesis, growth and polarity.

(A and B) *Quantification of lumen formation in spheroids grown from stable Caco-2 cells expressing the indicated MINA (A) or MPP6 (B) shRNA sequences. Bars represent the*

average percentage of spheroids with one central lumen of n = 5 (C) and n = 3 (D) independent experiments. The average of each condition is shown above each respective bar.
(C and D) *Quantification of size of spheroids grown from stable Caco-2 cells expressing the indicated MINA (C) or MPP6 (D) shRNA sequences. Horizontal lines represent the average spheroid diameter from n = 3 independent experiments. The average of each condition and the number of spheroids counted are shown below each respective beeswarm.*
(E and F) *MINA (E) and MPP6 (F) depletion reduces spheroid growth. Growth of spheroids was analyzed using a CellTiter-Glo Luminescent Cell Viability Assay kit after 3, 5 and 7 days in culture. Presented values are the average of n = 4 independent experiments. AU, arbitrary unit.*
(G and H) *MINA (G) and MPP6 (H) depletion prevent appropriate membrane localization of Claudin-1 and ZO-1. Representative immunofluorescence images of 3D Caco-2 spheroids expressing the indicated shRNAs and stained for Claudin-1 (magenta), ZO-1 (yellow), and DNA (DAPI, cyan). Scale bars, 20 µm.*
(I) *MPP6 C298A overexpression phenocopies MINA and MPP6 knockdown. Single cells were grown to spheroids for 7 days, fixed and stained for HA (MPP6, magenta) and tight junction marker ZO-1 (yellow). Nuclei were visualized with DAPI (cyan). Scale bars represent 10 µm.*
(A – D) *Statistical significance was determined using a one-way ANOVA and p values were calculated post-hoc using a Dunnett's multiple comparisons test. Error bars, SD.*

Overall, our data are consistent with MPP6 acting in a pathway downstream of extra-nucleolar MINA that regulates cell adhesion, barrier function, and morphogenesis. Because this pathway is suppressed by RNApol1 activity and the nucleolar proteome, the work identifies a novel link between ribosome biogenesis and epithelial membrane biology.

Discussion

Here in this paper, we have uncovered the extra-nucleolar function of the protein hydroxylase MINA, demonstrating, for the first time, that it controls epithelial TJ integrity, barrier function, and morphogenesis through its interaction with the MAGUK protein MPP6. In doing so we have discovered that cellular growth status and ribosome biogenesis are functionally coupled to the epithelial plasma membrane, via a novel nuclear partnership between MPP6 and the 2OG-oxygenase MINA (Figure 7). The work raises the intriguing possibility that ribosome biogenesis might also couple to membrane biology in other ways, and that other growth responsive cellular processes might sink proteins that would otherwise suppress such roles. Could the uniquely nutrient-dependent 2OG-oxygenase family play a more general role in signaling between subcellular compartments to couple cell systems controlling cell growth and differentiation?

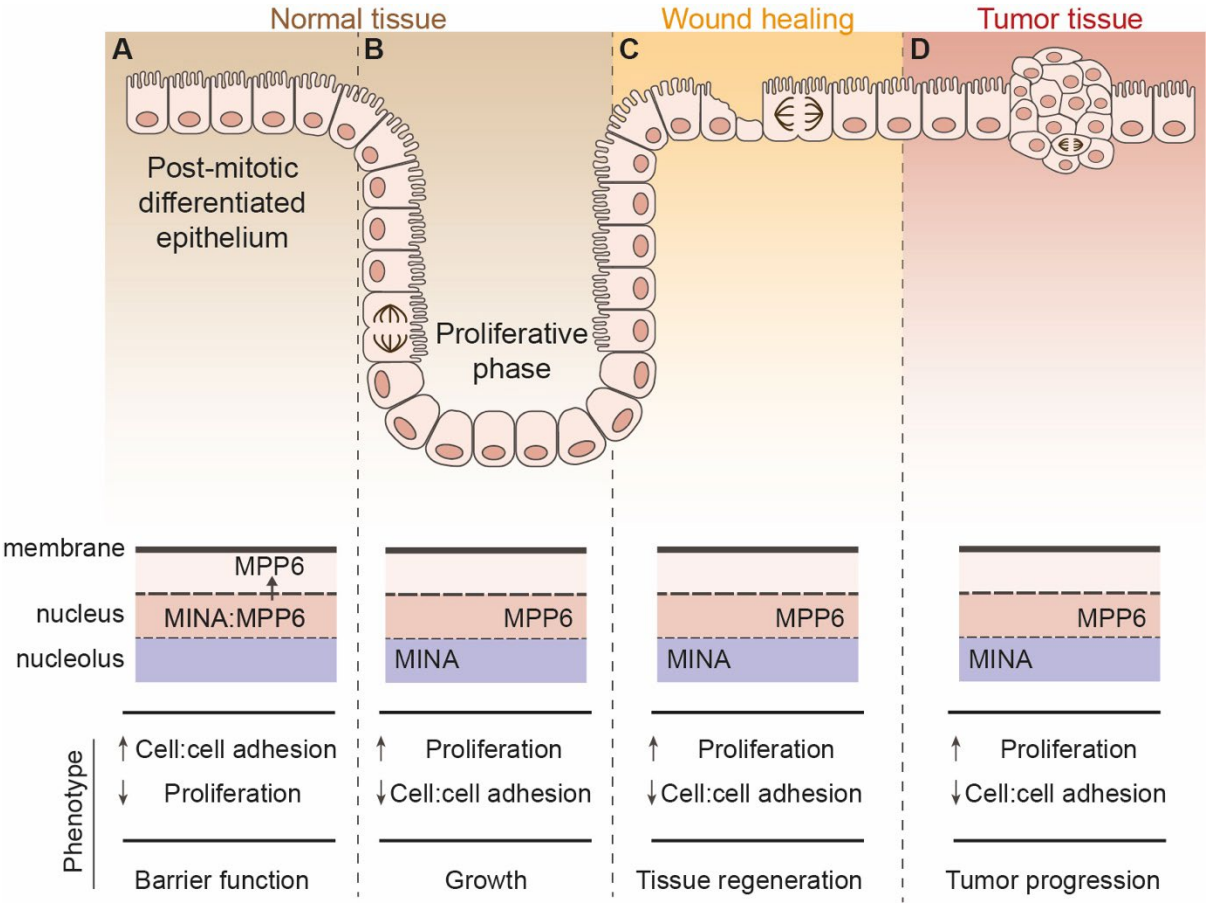

Figure 7. Model depicting the localization of MINA and MPP6 in different physiological and pathological contexts and the consequences on adhesion and barrier function.
*(**A**) In a healthy differentiated epithelium, cells have basal levels of ribosome biogenesis and MINA is mostly nucleoplasmic. Nuclear MINA binds MPP6 and promotes subsequent membrane localization of MPP6 and cell:cell adhesion, thus facilitating barrier function.*
*(**B-C**) To maintain tissue homeostasis (B) or upon injury (C) cells re(enter) the cell cycle. Increased ribosome biogenesis sequesters MINA in the nucleolus, where it drives RPL27a hydroxylation and supports cell growth. The corresponding reduction in nucleoplasmic MINA inhibits the MINA:MPP6 interaction and impairs membrane localization of MPP6, thereby inhibiting cell:cell adhesion to support cell growth and tissue morphogenesis.*
***(D)** Similar to a proliferative epithelium, as shown in (B) and (C), pathogenic signals such as oncogene activation trigger nucleolar localization of MINA, thereby suppressing cell adhesion and promoting tumor progression. In such contexts, RNA polymerase I inhibition is predicted to cause translocation of MINA into the nucleoplasm (i.e. a return to (A)), thereby 'normalizing' cell adhesion and barrier function.*
*(**A-D**) It should be noted that the intestinal epithelium is used for illustrative purposes only, and that this hypothesis could equally apply to other tissue types.*

600 Although 2OG-oxygenases are still considered an emerging enzyme family, relative to others
601 (such as kinases), they have already been implicated in a variety of essential cellular systems,
602 from oxygen sensing and epigenetics to protein translation and collagen synthesis (Islam et
603 al., 2018; Ploumakis and Coleman, 2015). These enzymes have not previously been
604 demonstrated to play a role in regulating cell polarity and adhesion through the direct
605 interaction with peripheral membrane proteins, however. Although the interaction with MPP6
606 was entirely dependent on the integrity of a critical Fe(II)-binding residue within the MINA
607 catalytic pocket (Figure 4), it did not result in a detectable hydroxylation event (Figures S9 and
608 S10). Although more work is required to definitively conclude that a modification is not
609 catalyzed, it is also possible that MPP6 is sensing the availability of the catalytic pocket as an
610 indicator of the absence of RPL27A and/or co-factors. Indeed, computational investigation of
611 potential MPP6 interaction modes suggests that the GPFCG region at the tip of the Hinge
612 domain (Figures 4E and S8F) might directly bind the MINA active site through formation of β-
613 turn like structures (Figure S13). Although 'pseudo-substrates' have been identified for other
614 enzyme classes, this may be one of the first potential candidates that we know of for the 2OG-
615 oxygenase family. As such, the work is relevant to the wider field: Protein hydroxylases,
616 including Hypoxia Inducible Factor prolyl hydroxylases, may be at risk of substrate
617 misassignment (Cockman et al., 2019), in part because of the artefactual oxidation of residues
618 such as tryptophan during MS sample preparation, as also demonstrated here (Figure S9).
619 Our work raises the possibility that some proteins that interact with the catalytic domain of
620 2OG-oxygenases may be doing so in a pseudo-substrate-like manner, rather than as prime
621 substrates.
622
623 Through our phenotypic and proteomic analyses of MINA, we have helped clarify the function
624 of the poorly characterized human MAGUK protein MPP6. The *drosophila* homologue of
625 MPP6 (*Varicose*) has been more extensively studied than its human counterpart: *Varicose* is
626 essential for the assembly and function of septate junctions (which are thought to be the
627 equivalent of vertebrate TJs) and for normal tracheal development (Moyer and Jacobs, 2008;
628 Wu et al., 2007). A similar role for MPP6 in TJ function in human cells is supported by our
629 results showing that its loss of function causes reduced dome and TEER formation and
630 decreased Claudin-1 expression (Figure 5). Under conditions of MINA or MPP6 knockdown
631 we did not observe widespread mis-localization of tight or adherens junction markers however,
632 particularly in 2D. Similar observations were made with *Varicose (Wu et al., 2007)* and with
633 other human polarity proteins, including MPP7, Scribble and Par3 (Qin et al., 2005; Stucke et
634 al., 2007; Xue et al., 2013). The prevailing hypothesis is that such proteins are not primarily
635 involved in the establishment of apico-basal cell polarity, but rather in ensuring and
636 maintaining junctional functionality. MINA appears to promote this function at least in part by

637 facilitating MPP6 membrane localization (Figures 5A and 5B), which could in turn support
638 normal expression (Figure 5C), as observed for other peripheral membrane proteins (e.g.
639 (Perdivara et al., 2010)). How MINA achieves this is not yet clear, although it seems likely that
640 this is a consequence of the direct interaction with the Hinge domain of MPP6 in the nucleus.
641 Although the function and interacting partners of the MPP6 Hinge domain are poorly
642 characterized, mutagenesis screens in the fly model demonstrate it is essential (Wu et al.,
643 2007). The Hinge domain of related human MAGUK proteins have been implicated in
644 membrane localization, protein-protein interactions, and proteasomal degradation (Hanada et
645 al., 2003; Moreno-García et al., 2010), consistent with the results described here. Further work
646 is required to explore how extra-nucleolar MINA supports the translocation of nuclear MPP6
647 to the plasma membrane to function in TJ biology.
648
649 TJs are critical for normal physiology and have been heavily implicated in disease (Buckley
650 and Turner, 2018; Krug et al., 2014; Sawada, 2013). Their barrier function plays a critical role
651 in regulating permeability to small molecules, immune cells, pathogens, and parasites, and as
652 such has been implicated in a wide variety of diseases across multiple tissues, including colitis,
653 infection, edema, and allergy (Buckley and Turner, 2018; Krug et al., 2014; Sawada, 2013). In
654 light of the results presented here, it will be of interest to study the role of the MINA-MPP6
655 pathway in these contexts. A single-nucleotide polymorphism in the MINA gene is associated
656 with increased risk of asthma in children (Chen et al., 2011), and MINA knockout reduces the
657 allergic response to inhaled allergens in mice (Mori et al., 2013). MINA knockout mice also
658 show increased clearance of parasitic gastrointestinal nematode worms (Pillai et al., 2019),
659 which in some contexts can be associated with increased barrier permeability that supports
660 the 'washer/sweeper' effect and/or immunological access (Bąska and Norbury, 2022; McKay
661 et al., 2017). Whether a deregulated MPP6-TJ pathway could play a role in these contexts is
662 of interest and warrants future investigation.
663
664 Alterations in cell:cell junctions and adhesion is a hallmark of cancer (Hanahan and Weinberg,
665 2011). Loss of tumor suppressor genes in TJ complexes and signaling pathways disrupts their
666 fence function, resulting in abnormal polarity and reduced cell:cell adhesion, which together
667 disrupt morphogenesis and promote migration/invasion (Martin and Jiang, 2009). Although
668 several mechanisms have been described by which TJs are rendered dysfunctional in
669 epithelial cancers, it is likely that others remain to be discovered: We propose that the MINA-
670 MPP6 pathway is one such candidate that is worthy of further investigation, for the following
671 reasons. Firstly, although MINA has been proposed as a biomarker and drug target in a range
672 of tumor types (reviewed in (Thakur and Chen, 2015)), there is emerging evidence supporting
673 a paradoxical and poorly characterized role in tumor suppression (Komiya et al., 2010; Yu et

674 al., 2014). Secondly, low MPP6 expression is associated with poor prognosis in some cancers,
675 and the MPP6 gene is located in a chromosomal region (7p15-21) altered in several tumor
676 types (Grundy et al., 1998; Miozzo et al., 1996; Parada et al., 1998; Powlesland et al., 2000;
677 Schmidt et al., 1999; Tseng et al., 2001; Wong et al., 1999; Xu et al., 2019). Thirdly, MPP6
678 interacts with Cell Adhesion Molecule 1 (CADM1), an immunoglobulin superfamily
679 transmembrane protein that is a tumor suppressor in a wide variety of cancers (Murakami,
680 2005) . Future work should focus on the mechanisms by which the MINA-MPP6 pathway may
681 be inactivated in cancer and the consequences of this on the barrier and fence functions of
682 TJs. Furthermore, the work presented here suggests that an important mechanism by which
683 the MINA-MPP6 pathway could be suppressed is through oncogene-induced nucleolar
684 sequestration of MINA due to elevated RNAPol1 activity and ribosome biogenesis (Figure 7).
685 RNAPol1 inhibitors are being considered as novel chemotherapeutics (reviewed in (Ferreira
686 et al., 2020)): Our hypothesis would predict that such treatments might not only negatively
687 impact growth and viability, but also help to 'normalize' cell:cell adhesion and polarity in some
688 contexts.
689

690 ## Methods

691 ### Plasmid constructs and cloning procedures

692 Coding sequences of MINA, MPP6 and NO66 were PCR cloned from plasmid DNA or cDNA
693 into pFLAG (Sigma), pEF6 (Invitrogen), pTIPZ, pIPZ or pIHZ vectors. pIPZ and pTIPZ are
694 derivatives of the pGIPZ and pTRIPZ lentiviral vectors (Open Biosystems) that lack green
695 fluorescent protein (GFP) and red fluorescent protein (RFP), respectively. The coding
696 sequences of MPP2 and MPP2/6 hybrids containing C-terminal HA-tags and restriction sites
697 required for cloning into the pIPZ vector were obtained from Thermo Scientific as GeneArt
698 String Fragment. Non-targeting control (ULTRA-NT#4), MINA (ULTRA-3406274, ULTRA-
699 3406273) and MPP6 (ULTRA-3337606, ULTRA-3337607) shRNA sequences in pZIP-TRE3G
700 vectors were obtained from TransOMIC. PCR reactions were driven by the Phusion High
701 Fidelity DNA polymerase (New England Biolabs (NEB), M0530). Primers were designed to
702 contain a C- or N-terminal tag and the required restriction sites for subsequent ligations.
703 Constructs were confirmed by sequencing, carried out by Source Bioscience. For nucleotide
704 exchanges, site-directed mutagenesis was performed using a Phusion Site-directed
705 Mutagenesis kit (Thermo, F541). 5' termini of the primers were phosphorylated using T4
706 polynucleotide kinase (PNK, Thermo, EK0031) prior to the reactions. All constructs were
707 confirmed by sequencing.

708

709 **Cell culture**

710 HEK293T, Caco-2, SW620 and U2OS cells were cultured in Dulbecco's Modified Eagle
711 Medium (DMEM, Gibco) supplemented with 10% (v/v) fetal bovine serum (FBS, Sigma) and
712 100 international units/mL (IU/mL) penicillin and 100 µg/mL streptomycin (Gibco). Cell culture
713 medium for stable cell lines was supplemented with 1 µg/mL puromycin (Gibco). For 3D
714 spheroid cultures, Caco-2 cells were seeded into Matrigel-coated (Corning, 35621) chamber
715 slides and the culturing medium was supplemented with 4% (v/v) Matrigel. All cell lines were
716 grown at 37°C in a humidified atmosphere with 5% (v/v) CO_2. All cell lines were regularly
717 tested for mycoplasma contamination using a LookOut® Mycoplasma PCR Detection kit
718 (Sigma, MP0036).

719 Where doxycycline-inducible shRNA cell lines were used for experiments, shRNA expression
720 was induced using 1 µg/mL doxycycline (Sigma, D9891) for 72 h before seeding.
721 Subsequently, the culturing medium was refreshed, and fresh doxycycline was added every
722 48-72 h.

723 **Transient transfection**

724 Plasmid DNA transfections were performed using FuGENE® 6 transfection reagent
725 (Promega). Briefly, the transfections mix was made up in Opti-MEM™ (Gibco, 31985070)
726 using a ratio of DNA to transfection reagent of 1:3 and incubated for 15-30 min at room
727 temperature (RT) before the complexes were added to the cells. 500 ng of DNA was used per
728 mL of culturing medium. Cells were seeded 24 h before transfection and lysed or fixed 48 h
729 after transfection.

730 **Generation of stable cell lines**

731 Stable expression cell lines were generated by transduction with lentivirus. For lentivirus
732 production, HEK293T cells were transfected with the plasmid of interest (50%), the packaging
733 vector psPAX2 (35%) and envelope vector pMD2.G (15%) as described above. The lentivirus-
734 containing supernatant was collected 48 h after transfection, passed through a 0.45 µM
735 polyethersulfone (PES) filter, diluted 1:1 with fresh medium and added to the recipient cells
736 for 48 h. Thereafter, transduced cells were selected using puromycin (2 µg/mL final
737 concentration, Gibco).

738 **Metabolic labelling of newly synthesized proteins**

739 Protein synthesis was monitored with L-azidohomoalanine (AHA) using a Click-iT™ Nascent
740 Protein Synthesis kit (Thermo Scientific) according to the instructions of the manufacturer.
741 Briefly, cells were incubated with methionine-free medium for 1 h before AHA was added at a
742 final concentration of 50 mM. After 1 h, cells were fixed and permeabilized as described below.

743 Next, Alexa Fluor 595 Alkyne diluted in Click-iT® Cell Reaction Buffer (Thermo Scientific) at a
744 final concentration of 2.5 mM was conjugated to any incorporated AHA.

745 **Proximity ligation assay**

746 Duolink® proximity ligation assay kits were purchased from Sigma-Aldrich and performed
747 according to the manufacturer's instructions.

748 **Immunofluorescence staining**

749 For immunofluorescence studies of 2D cultures, cells were grown on poly-D-lysine-coated or
750 uncoated glass coverslips and fixed or 4% (w/v) paraformaldehyde (PFA) for 15 min at RT
751 with methanol for 10 min at -20°C. Where methanol was used, it is stated in the figure caption.
752 Cells fixed with PFA were subsequently permeabilized using 0.1% (v/v) Triton in PBS for 10
753 min at RT. Next, cells were blocked with 1% (w/v) bovine serum albumin (BSA) in PBS for 1
754 h at RT and subsequently incubated overnight (ON) at 4°C with primary antibodies diluted in
755 1% (w/v) BSA in PBS. The following primary antibodies were used: FLAG (Sigma, F1804,
756 1:1,000), HA (Covance, MMS-101P, 1:500), HA (Cell Signaling Technology (CST), C29F4,
757 1:500), nucleolin (Santa Cruz Biotechnology (SCB), sc-13056, 1:200-1:1,000),
758 nucleophosmin-1 (SCB, sc-6013-R, 1:200), MINA (Invitrogen, 39-7300, 1:100), Claudin-1
759 (Abcam, ab211737, 1:500), β-catenin (BD Transduction Laboratories, 610153, 1:500). The
760 next day, coverslips were washed with 1% (w/v) BSA in PBS and incubated with secondary
761 antibodies diluted in 1% (w/v) BSA in PBS for 1 h at RT. Alexa Fluor 488, 555 or 633 secondary
762 antibodies were purchased from Invitrogen and used at a final concentration of 1:1,000. Nuclei
763 were stained by incubation with 0.5 – 1 µg/mL 4',6-diamidino-2-phenylindole (DAPI, D1306,
764 Invitrogen) in PBS for 10 min at RT, and the coverslips were mounted with Prolong Gold
765 antifade mountant (Molecular Probes) onto microscope slides.

766 Caco-2 cells grown as 3D cultures were fixed with 4% (w/v) PFA/5% (w/v) sucrose in PBS for
767 20 min at RT, washed 3 times with PBS and incubated with 100 mM glycine in PBS for 20 min
768 at RT to quench unreacted aldehydes. Subsequent permeabilization, blocking and staining
769 were performed as described above. Stained spheroids were stored in PBS at 4°C until they
770 were imaged.

771 **Image acquisition, processing and quantification**

772 Confocal images were acquired using a Zeiss LSM 780 or 880 laser scanning confocal system
773 equipped with a 20x, 40x or 60 C-Apochromat 1.2 W Korr M27 objective. Immunofluorescence
774 images of similarly stained experiments were acquired with identical laser power and detector
775 gain. Images were processed using Fiji software (https://fiji.sc) and arranged in Adobe

776 Illustrator. Brightness and contrast were adjusted using only linear operations applied to the
777 entire image.

778 Cell perimeters were measured using the CellMorph plugin for Fiji
779 (https://github.com/viboud12/CellMorph). Ten random images were taken for each condition
780 in each experiment. Quantification was based on ZO-1 staining.

781 Phase-contrast images were acquired using an EVOS™ FL color imaging system equipped
782 with a 4x or 10x Plan PH2 objective. To quantify domes, a total of 30 phase-contrast images
783 were taken per condition per experiment, 4 or 5 days after seeding when the cells had formed
784 a confluent monolayer. To quantify spheroids, a total of 10 images were taken per condition
785 per experiment, 7 days after seeding.

786 **Transepithelial electrical resistance measurements**

787 Caco-2 cells were seeded onto cellQART® permeable support inserts (0.4 mm pore size).
788 The transepithelial electrical resistance (TEER) was measured using an EVOM2 epithelial
789 voltohmmeter (World Precision Instruments, Inc.) and a STX2 electrode (World Precision
790 Instruments, Inc.) according to the manufacturer's instructions. Background resistance was
791 measured using cell-free inserts. Three measurements were taken for each sample at each
792 time point.

793 **Whole cell extracts**

794 Cells were washed and harvested in ice-cold PBS, pelleted by centrifugation at 234 x g and
795 lysed by rotation at 4°C for 1 h in JIES buffer (100 mM NaCl, 20 mM Tris-HCl [pH 7.4], 5 mM
796 MgCl2, 0.5% (v/v) NP-40) containing 1x SIGMAFAST protease inhibitor cocktail (Sigma-
797 Aldrich, S8830). Subsequently, cell debris was pelleted by centrifugation (10 min at 21,910 x
798 g at 4°C) and the supernatant was collected. Protein concentration was determined using
799 Pierce™ 660nm Protein Assay Reagent according to the manufacturer's instructions (Thermo,
800 22660). Finally, protein samples were prepared at equal concentrations in 1x Laemmli Loading
801 Buffer (6x: 125 mM Tris-HCl [pH 6.8], 6% (w/v) SDS, 50% (v/v) glycerol, 225 mM dithiotheitol
802 (DTT), 0.1% (w/v) bromophenol blue) and boiled for 5 min. 3D cell cultures were harvested in
803 ice-cold PBS containing 1x SIGMAFAST protease inhibitor cocktail, pelleted by centrifugation
804 at 21,910 x g at 4°C and washed 3 times with PBS containing 1x SIGMAFAST protease
805 inhibitor cocktail to remove the Matrigel. Subsequently, the cell pellets were resuspended in
806 1x Laemmli Loading Buffer, boiled for 5 min and sonicated.

807 **Immunoprecipitation**

808 For immunoprecipitations, cells were harvested on ice and lysed by rotation for 1 h at 4°C in
809 JIES buffer (see above) containing 1x SIGMAFAST protease inhibitor cocktail (Sigma-Aldrich,

810 S8830). Subsequently, cell debris was pelleted by centrifugation (10 min at 21,910 x g at 4°C)
811 and the supernatant was incubated with anti-FLAG® M2 Magnetic Beads (Sigma-Aldrich,
812 M8823) or anti-hemagglutinin (HA) agarose beads (Sigma-Aldrich, A2095) overnight at 4°C.
813 The next day, beads were washed 6 times with JIES buffer before the immunoprecipitates
814 were boiled for 5 min in 1x Laemmli Loading Buffer or eluted using 100 µg/mL HA (Thermo
815 Scientific, 26184) or 40 ng/mL FLAG (Generon, A6001) peptide in JIES for 15 min at 1,400
816 rpm at RT.

817 **SDS-PAGE and immunoblot analysis**

818 Protein lysates were resolved by sodium dodecyl-sulfate polyacrylamide gel electrophoresis
819 (SDS-PAGE). Protein samples prepared in Laemmli Loading Buffer (see above) were loaded
820 onto either 10%, 12% or 15% (v/v) polyacrylamide gels made in-house, Novex WedgeWell 8-
821 16% gels (Invitrogen, XP08165BOX) or NuPAGE 4-12% Bis-Tris Midi gels (Invitrogen,
822 WG1403A). Electrophoresis was performed in Tris/Glycine/SDS (National diagnostics) or
823 NuPAGE MOPS SDS (Invitrogen, cat. no. NP0001) running buffer. Following SDS-PAGE, the
824 samples were electroblotted onto methanol-activated Amersham Hybond P0.45
825 polyvinylidene difluoride (PVDF) membranes (GE Healthcare) in Tris/Glycine transfer buffer
826 (National diagnostics). Following transfer, the membrane was blocked with 5% (w/v) milk
827 powder dissolved in PBS/0.1% (v/v) Tween-20 (PBS-T) and incubated with primary antibody
828 for 1 h at RT or overnight at 4°C. Where unconjugated primary antibodies were used,
829 immunoblots were subsequently incubated with horseradish peroxidase (HRP)-conjugated
830 secondary antibodies purchased from Cell Signaling. Signals were visualized using Clarity
831 Western ECL reagent (Bio-Rad) or Femto (Thermo Scientific) using a Vilber Fusion Fx. The
832 following primary antibodies were used: FLAG-HRP (Sigma, A8592, 1:10,000), β-actin-HRP
833 (Abcam, ab49900, 1:25,000), HA-HRP (Roche, 12013819001, 1:1,000-1:5,000), MPP6 (Atlas
834 antibodies, HPA019085, 1:500), RPL27A (Abcam, ab74731, 1:500), LIN7C (Proteintech,
835 14656-1-AP, 1:1000), MINA (DSHB, 6C6, 1:40), Claudin-1 (Abcam, ab211737, 1:1000).

836 **Mass spectrometry**

837 MPP6-3xFLAG was anti-FLAG immunopurified from overexpressing HEK293T cells and
838 eluted with 3XFLAG peptide, as outlined above. Samples were extracted, in-solution digested
839 with chymotrypsin, desalted, and analyzed by mass spectrometry as described previously
840 (Markolovic et al., 2018). Data were searched against the UniProt Reference Homo sapiens
841 database with PEAKS Studio X Software (Bioinformatics Solutions). Cysteine
842 carbamidomethylation was selected as a 'fixed' modification, with oxidation (M), deamidation
843 (N, Q) and hydroxylation (P, K, D, N, R, Y, H, W) as variable modifications. The data were

844 then filtered to remove methionine oxidations and those with an A-score of <20 (an A-score of
845 20 corresponds to a modification correctly localized with 99% certainty).

846 ***In vitro* hydroxylation assays**

847 For *in vitro* hydroxylation assays, HA-tagged MINA was overexpressed and purified from
848 HEK293T cells, as described above. Following immunoprecipitation, the purified protein was
849 eluted using 2 µg/mL HA peptide (Thermo Scientific, 26184) in 50 mM HEPES, 50 mM NaCl.
850 Purified enzyme was then incubated with RPL27A peptide (GRGNAGGLHHHINFDKYHP) at
851 a final concentration of 100 µM in 50 mM Tris [pH 7.5], 150 mM NaCl, 1 mM DTT for 5 min at
852 37°C in the presence of 200 µM 2OG, 100 µM Fe(II) and 100 µM ascorbate (final volume 20
853 µL). For peptide competition assays HA-MINA was incubated with a combination of 50 µM of
854 RPL27A peptide and 50 µM of Rpl8 peptide (NPVEHPFGGGNHQHIGKPSTI) or 50 µM of
855 MPP6 peptide (SQFLEEKRKAFVRRDWDNSGPFCGTISSKKKKK) and incubated for 30 min
856 at 37°C. Thereafter, the reaction was quenched with 10 µL of 1% (v/v) formic acid (HCOOH)
857 in H_2O. The presence of hydroxylation was subsequently analyzed using a Succinate-Glo
858 JmjC Demethylase/Hydroxylase Assay kit (Promega), as follows. Samples were diluted 1:10
859 in H_2O and 5 µL of the diluted reaction was mixed with an equal volume of Succinate-Glo
860 detection reagent 1 and incubated for 1 h at RT in a clear bottom 384-well plate. Each reaction
861 was performed in triplicate. Subsequently, 10 µL of Succinate-Glo detection reagent 2 was
862 added, mixed and incubated for 10 min at RT, before luminescence was analyzed.

863 **Structural analysis**

864 Molecular modelling and structural comparisons were carried out using the SSM superposition
865 facility (Krissinel and Henrick, 2004) in Coot (Emsley and Cowtan, 2004) and visualized in
866 PyMOL (The PyMOL Molecular Graphics System, Version 1.2r3pre, Schrödinger, LLC).
867 Coordinates for human MPP6 full-length were obtained either from the AlphaFold database or
868 generated *ab initio* using the ColabFold server (Mirdita et al., 2022).

869 **Statistical analysis**

870 Statistical analyses were performed in R. Statistical significance was determined using
871 unpaired t test or one-way analysis of variance (ANOVA) followed by a Dunnett's test or
872 pairwise t tests with Benjamini-Hochberg correction for multiple comparisons. Differences
873 were considered significant at $p<0.05$. Calculated *p* values are shown in each graph. Sample
874 sizes were chosen empirically. Western blot quantifications were performed with Fiji.

875

Acknowledgements

We thank Marion Schmidt-Zachmann (DKFZ, Heidelberg) for the MINA antibody and Peter Ratcliffe, Matthew Cockman and Sally Roberts for critical reading of the manuscript. E.H. was supported by a BBSRC-MIBTP award to E.H. and M.L.C (1790845). E.H, R.A. and U.B. were funded by a Cancer Research UK Programme Foundation Award to M.L.C. (C33483/A2567). S.J.S. is supported by a transitional award from the Francis Crick Institute (CR2019/003DK). The work was also supported by an MRC project grant to M.L.C. (MR/N021053/1).

Author contributions

E.H. and R.A. designed and performed the experiments, analyzed the data and generated the figures. A.K contributed to generation of data. U.B., J.R.B. and A.Z. contributed to molecular biology. R.H. and R.F. performed mass spectrometry analysis. E.H. and M.L.C wrote the manuscript. M.L.C. co-designed the experiments and directed the project. S.J.S. performed structural analyses. All authors approved the final version of the manuscript.

Competing interests

The authors declare no competing interests.

References

Andersen, J.S., Lam, Y.W., Leung, A.K., Ong, S.E., Lyon, C.E., Lamond, A.I., and Mann, M. (2005). Nucleolar proteome dynamics. Nature *433*, 77-83.

Arabi, A., Wu, S., Ridderstråle, K., Bierhoff, H., Shiue, C., Fatyol, K., Fahlén, S., Hydbring, P., Söderberg, O., Grummt, I.*, et al.* (2005). c-Myc associates with ribosomal DNA and activates RNA polymerase I transcription. Nat Cell Biol *7*, 303-310.

Bąska, P., and Norbury, L.J. (2022). The Role of the Intestinal Epithelium in the "Weep and Sweep" Response during Gastro-Intestinal Helminth Infections. Animals (Basel) *12*.

Buckley, A., and Turner, J.R. (2018). Cell Biology of Tight Junction Barrier Regulation and Mucosal Disease. Cold Spring Harb Perspect Biol *10*.

Bundred, J.R., Hendrix, E., and Coleman, M.L. (2018). The emerging roles of ribosomal histidyl hydroxylases in cell biology, physiology and disease. Cellular and molecular life sciences : CMLS *75*, 4093-4105.

Chen, Y., Yang, X., Huang, Y., Liu, E., and Wang, L. (2011). Associations of the single-nucleotide polymorphisms of the Mina gene with the development of asthma in Chinese Han children: a case-control study. Genet Test Mol Biomarkers *15*, 531-536.

Chowdhury, R., Sekirnik, R., Brissett, N.C., Krojer, T., Ho, C.H., Ng, S.S., Clifton, I.J., Ge, W., Kershaw, N.J., Fox, G.C.*, et al.* (2014). Ribosomal oxygenases are structurally conserved from prokaryotes to humans. Nature *510*, 422-426.

Chytła, A., Gajdzik-Nowak, W., Olszewska, P., Biernatowska, A., Sikorski, A.F., and Czogalla, A. (2020). Not Just Another Scaffolding Protein Family: The Multifaceted MPPs. Molecules *25*.

Cockman, M.E., Lancaster, D.E., Stolze, I.P., Hewitson, K.S., McDonough, M.A., Coleman, M.L., Coles, C.H., Yu, X., Hay, R.T., Ley, S.C*., et al.* (2006). Posttranslational hydroxylation of ankyrin repeats in IkappaB proteins by the hypoxia-inducible factor (HIF) asparaginyl hydroxylase, factor inhibiting HIF (FIH). Proceedings of the National Academy of Sciences of the United States of America *103*, 14767-14772.

Cockman, M.E., Lippl, K., Tian, Y.M., Pegg, H.B., Figg, W.D.J., Abboud, M.I., Heilig, R., Fischer, R., Myllyharju, J., Schofield, C.J*., et al.* (2019). Lack of activity of recombinant HIF prolyl hydroxylases (PHDs) on reported non-HIF substrates. Elife *8*.

Coleman, M.L., McDonough, M.A., Hewitson, K.S., Coles, C., Mecinovic, J., Edelmann, M., Cook, K.M., Cockman, M.E., Lancaster, D.E., Kessler, B.M*., et al.* (2007). Asparaginyl hydroxylation of the Notch ankyrin repeat domain by factor inhibiting hypoxia-inducible factor. The Journal of biological chemistry *282*, 24027-24038.

Eilbracht, J., Kneissel, S., Hofmann, A., and Schmidt-Zachmann, M.S. (2005). Protein NO52--a constitutive nucleolar component sharing high sequence homologies to protein NO66. Eur J Cell Biol *84*, 279-294.

Emsley, P., and Cowtan, K. (2004). Coot: model-building tools for molecular graphics. Acta Crystallogr D Biol Crystallogr *60*, 2126-2132.

Feng, T., Yamamoto, A., Wilkins, S.E., Sokolova, E., Yates, L.A., Munzel, M., Singh, P., Hopkinson, R.J., Fischer, R., Cockman, M.E*., et al.* (2014). Optimal translational termination requires C4 lysyl hydroxylation of eRF1. Molecular cell *53*, 645-654.

Ferreira, R., Schneekloth, J.S., Jr., Panov, K.I., Hannan, K.M., and Hannan, R.D. (2020). Targeting the RNA Polymerase I Transcription for Cancer Therapy Comes of Age. Cells *9*.

Ge, W., Wolf, A., Feng, T., Ho, C.H., Sekirnik, R., Zayer, A., Granatino, N., Cockman, M.E., Loenarz, C., Loik, N.D*., et al.* (2012). Oxygenase-catalyzed ribosome hydroxylation occurs in prokaryotes and humans. Nat Chem Biol *8*, 960-962.

Grandori, C., Gomez-Roman, N., Felton-Edkins, Z.A., Ngouenet, C., Galloway, D.A., Eisenman, R.N., and White, R.J. (2005). c-Myc binds to human ribosomal DNA and stimulates transcription of rRNA genes by RNA polymerase I. Nat Cell Biol *7*, 311-318.

Grundy, R.G., Pritchard, J., Scambler, P., and Cowell, J.K. (1998). Loss of heterozygosity for the short arm of chromosome 7 in sporadic Wilms tumour. Oncogene *17*, 395-400.

Hanada, T., Takeuchi, A., Sondarva, G., and Chishti, A.H. (2003). Protein 4.1-mediated membrane targeting of human discs large in epithelial cells. J Biol Chem *278*, 34445-34450.

Hanahan, D., and Weinberg, R.A. (2011). Hallmarks of cancer: the next generation. Cell *144*, 646-674.

Islam, M.S., Leissing, T.M., Chowdhury, R., Hopkinson, R.J., and Schofield, C.J. (2018). 2-Oxoglutarate-Dependent Oxygenases. Annu Rev Biochem *87*, 585-620.

Jaffe, A.B., Kaji, N., Durgan, J., and Hall, A. (2008). Cdc42 controls spindle orientation to position the apical surface during epithelial morphogenesis. J Cell Biol *183*, 625-633.

Jones, M.C., Zha, J., and Humphries, M.J. (2019). Connections between the cell cycle, cell adhesion and the cytoskeleton. Philos Trans R Soc Lond B Biol Sci *374*, 20180227.

Komiya, K., Sueoka-Aragane, N., Sato, A., Hisatomi, T., Sakuragi, T., Mitsuoka, M., Sato, T., Hayashi, S., Izumi, H., Tsuneoka, M*., et al.* (2010). Expression of Mina53, a novel c-Myc target gene, is a favorable prognostic marker in early stage lung cancer. Lung Cancer *69*, 232-238.

Krissinel, E., and Henrick, K. (2004). Secondary-structure matching (SSM), a new tool for fast protein structure alignment in three dimensions. Acta Crystallogr D Biol Crystallogr *60*, 2256-2268.

Krug, S.M., Schulzke, J.D., and Fromm, M. (2014). Tight junction, selective permeability, and related diseases. Semin Cell Dev Biol *36*, 166-176.

MacCallum, A., Hardy, S.P., and Everest, P.H. (2005). Campylobacter jejuni inhibits the absorptive transport functions of Caco-2 cells and disrupts cellular tight junctions. Microbiology (Reading) *151*, 2451-2458.

Markolovic, S., Zhuang, Q., Wilkins, S.E., Eaton, C.D., Abboud, M.I., Katz, M.J., McNeil, H.E., Lesniak, R.K., Hall, C., Struwe, W.B*., et al.* (2018). The Jumonji-C oxygenase JMJD7 catalyzes (3S)-lysyl hydroxylation of TRAFAC GTPases. Nat Chem Biol *14*, 688-695.

970 Martin, T.A., and Jiang, W.G. (2009). Loss of tight junction barrier function and its role in
971 cancer metastasis. Biochim Biophys Acta *1788*, 872-891.
972 McKay, D.M., Shute, A., and Lopes, F. (2017). Helminths and intestinal barrier function. Tissue
973 Barriers *5*, e1283385.
974 Miozzo, M., Perotti, D., Minoletti, F., Mondini, P., Pilotti, S., Luksch, R., Fossati-Bellani, F.,
975 Pierotti, M.A., Sozzi, G., and Radice, P. (1996). Mapping of a putative tumor suppressor locus
976 to proximal 7p in Wilms tumors. Genomics *37*, 310-315.
977 Mirdita, M., Schütze, K., Moriwaki, Y., Heo, L., Ovchinnikov, S., and Steinegger, M. (2022).
978 ColabFold: making protein folding accessible to all. Nat Methods *19*, 679-682.
979 Moreno-García, M.E., Sommer, K., Shinohara, H., Bandaranayake, A.D., Kurosaki, T., and
980 Rawlings, D.J. (2010). MAGUK-controlled ubiquitination of CARMA1 modulates lymphocyte
981 NF-kappaB activity. Mol Cell Biol *30*, 922-934.
982 Mori, T., Okamoto, K., Tanaka, Y., Teye, K., Umata, T., Ohneda, K., Tokuyama, K., Okabe,
983 M., and Tsuneoka, M. (2013). Ablation of Mina53 in mice reduces allergic response in the
984 airways. Cell Struct Funct *38*, 155-167.
985 Moyer, K.E., and Jacobs, J.R. (2008). Varicose: a MAGUK required for the maturation and
986 function of Drosophila septate junctions. BMC Dev Biol *8*, 99.
987 Murakami, Y. (2005). Involvement of a cell adhesion molecule, TSLC1/IGSF4, in human
988 oncogenesis. Cancer Sci *96*, 543-552.
989 Parada, L.A., Hallén, M., Tranberg, K.G., Hägerstrand, I., Bondeson, L., Mitelman, F., and
990 Johansson, B. (1998). Frequent rearrangements of chromosomes 1, 7, and 8 in primary liver
991 cancer. Genes Chromosomes Cancer *23*, 26-35.
992 Pelletier, J., Thomas, G., and Volarević, S. (2018). Ribosome biogenesis in cancer: new
993 players and therapeutic avenues. Nat Rev Cancer *18*, 51-63.
994 Perdivara, I., Deterding, L.J., Przybylski, M., and Tomer, K.B. (2010). Mass spectrometric
995 identification of oxidative modifications of tryptophan residues in proteins: chemical artifact or
996 post-translational modification? J Am Soc Mass Spectrom *21*, 1114-1117.
997 Pillai, M.R., Mihi, B., Ishiwata, K., Nakamura, K., Sakuragi, N., Finkelstein, D.B., McGargill,
998 M.A., Nakayama, T., Ayabe, T., Coleman, M.L.*, et al.* (2019). Myc-induced nuclear antigen
999 constrains a latent intestinal epithelial cell-intrinsic anthelmintic pathway. PLoS One *14*,
1000 e0211244.
1001 Ploumakis, A., and Coleman, M.L. (2015). OH, the Places You'll Go! Hydroxylation, Gene
1002 Expression, and Cancer. Molecular cell *58*, 729-741.
1003 Powlesland, R.M., Charles, A.K., Malik, K.T., Reynolds, P.A., Pires, S., Boavida, M., and
1004 Brown, K.W. (2000). Loss of heterozygosity at 7p in Wilms' tumour development. Br J Cancer
1005 *82*, 323-329.
1006 Qin, Y., Capaldo, C., Gumbiner, B.M., and Macara, I.G. (2005). The mammalian Scribble
1007 polarity protein regulates epithelial cell adhesion and migration through E-cadherin. J Cell Biol
1008 *171*, 1061-1071.
1009 Rossetti, S., Hoogeveen, A.T., Esposito, J., and Sacchi, N. (2010). Loss of MTG16a
1010 (CBFA2T3), a novel rDNA repressor, leads to increased ribogenesis and disruption of breast
1011 acinar morphogenesis. J Cell Mol Med *14*, 1358-1370.
1012 Rossetti, S., Wierzbicki, A.J., and Sacchi, N. (2016). Mammary epithelial morphogenesis and
1013 early breast cancer. Evidence of involvement of basal components of the RNA Polymerase I
1014 transcription machinery. Cell Cycle *15*, 2515-2526.
1015 Sambuy, Y., De Angelis, I., Ranaldi, G., Scarino, M.L., Stammati, A., and Zucco, F. (2005).
1016 The Caco-2 cell line as a model of the intestinal barrier: influence of cell and culture-related
1017 factors on Caco-2 cell functional characteristics. Cell Biol Toxicol *21*, 1-26.
1018 Sawada, N. (2013). Tight junction-related human diseases. Pathol Int *63*, 1-12.
1019 Schmidt, H., Würl, P., Taubert, H., Meye, A., Bache, M., Holzhausen, H.J., and Hinze, R.
1020 (1999). Genomic imbalances of 7p and 17q in malignant peripheral nerve sheath tumors are
1021 clinically relevant. Genes Chromosomes Cancer *25*, 205-211.
1022 Scott, M.S., Boisvert, F.M., McDowall, M.D., Lamond, A.I., and Barton, G.J. (2010).
1023 Characterization and prediction of protein nucleolar localization sequences. Nucleic Acids Res
1024 *38*, 7388-7399.

1025 Scott, M.S., Troshin, P.V., and Barton, G.J. (2011). NoD: a Nucleolar localization sequence
1026 detector for eukaryotic and viral proteins. BMC Bioinformatics *12*, 317.
1027 Srinivasan, B., Kolli, A.R., Esch, M.B., Abaci, H.E., Shuler, M.L., and Hickman, J.J. (2015).
1028 TEER measurement techniques for in vitro barrier model systems. J Lab Autom *20*, 107-126.
1029 Stucke, V.M., Timmerman, E., Vandekerckhove, J., Gevaert, K., and Hall, A. (2007). The
1030 MAGUK protein MPP7 binds to the polarity protein hDlg1 and facilitates epithelial tight junction
1031 formation. Mol Biol Cell *18*, 1744-1755.
1032 Thakur, C., and Chen, F. (2015). Current understanding of mdig/MINA in human cancers.
1033 Genes Cancer *6*, 288-302.
1034 Tseng, T.C., Marfatia, S.M., Bryant, P.J., Pack, S., Zhuang, Z., O'Brien, J.E., Lin, L., Hanada,
1035 T., and Chishti, A.H. (2001). VAM-1: a new member of the MAGUK family binds to human
1036 Veli-1 through a conserved domain. Biochim Biophys Acta *1518*, 249-259.
1037 Tsuneoka, M., Koda, Y., Soejima, M., Teye, K., and Kimura, H. (2002). A novel myc target
1038 gene, mina53, that is involved in cell proliferation. J Biol Chem *277*, 35450-35459.
1039 Tsuneoka, M., Nishimune, Y., Ohta, K., Teye, K., Tanaka, H., Soejima, M., Iida, H., Inokuchi,
1040 T., Kimura, H., and Koda, Y. (2006). Expression of Mina53, a product of a Myc target gene in
1041 mouse testis. Int J Androl *29*, 323-330.
1042 van Riggelen, J., Yetil, A., and Felsher, D.W. (2010). MYC as a regulator of ribosome
1043 biogenesis and protein synthesis. Nat Rev Cancer *10*, 301-309.
1044 Verrastro, I., Pasha, S., Jensen, K.T., Pitt, A.R., and Spickett, C.M. (2015). Mass
1045 Spectrometry-Based Methods for Identifying Oxidized Proteins in Disease: Advances and
1046 Challenges. Biomolecules *5*, 378-411.
1047 Wong, K.F., So, C.C., and Kwong, Y.L. (1999). Chronic myelomonocytic leukemia with
1048 t(7;11)(p15;p15) and NUP98/HOXA9 fusion. Cancer Genet Cytogenet *115*, 70-72.
1049 Wu, V.M., Yu, M.H., Paik, R., Banerjee, S., Liang, Z., Paul, S.M., Bhat, M.A., and Beitel, G.J.
1050 (2007). Drosophila Varicose, a member of a new subgroup of basolateral MAGUKs, is required
1051 for septate junctions and tracheal morphogenesis. Development *134*, 999-1009.
1052 Xu, F., Si, X., Du, J., Xu, F., Yang, A., Zhang, C., Zhang, X., and Yang, Y. (2019).
1053 Downregulating SynCAM and MPP6 expression is associated with ovarian cancer
1054 progression. Oncol Lett *18*, 2477-2483.
1055 Xue, B., Krishnamurthy, K., Allred, D.C., and Muthuswamy, S.K. (2013). Loss of Par3
1056 promotes breast cancer metastasis by compromising cell-cell cohesion. Nat Cell Biol *15*, 189-
1057 200.
1058 Yang, M., Chowdhury, R., Ge, W., Hamed, R.B., McDonough, M.A., Claridge, T.D., Kessler,
1059 B.M., Cockman, M.E., Ratcliffe, P.J., and Schofield, C.J. (2011a). Factor-inhibiting hypoxia-
1060 inducible factor (FIH) catalyses the post-translational hydroxylation of histidinyl residues within
1061 ankyrin repeat domains. The FEBS journal *278*, 1086-1097.
1062 Yang, M., Ge, W., Chowdhury, R., Claridge, T.D., Kramer, H.B., Schmierer, B., McDonough,
1063 M.A., Gong, L., Kessler, B.M., Ratcliffe, P.J.*, et al.* (2011b). Asparagine and aspartate
1064 hydroxylation of the cytoskeletal ankyrin family is catalyzed by factor-inhibiting hypoxia-
1065 inducible factor. The Journal of biological chemistry *286*, 7648-7660.
1066 Yanshina, D.D., Gopanenko, A.V., Karpova, G.G., and Malygin, A.A. (2020). [Replacement of
1067 Hydroxylated His39 in Ribosomal Protein uL15 with Ala or Thr Impairs the Translational
1068 Activity of Human Ribosomes]. Mol Biol (Mosk) *54*, 512-521.
1069 Ye, F., Zeng, M., and Zhang, M. (2018). Mechanisms of MAGUK-mediated cellular junctional
1070 complex organization. Curr Opin Struct Biol *48*, 6-15.
1071 Yu, M., Sun, J., Thakur, C., Chen, B., Lu, Y., Zhao, H., and Chen, F. (2014). Paradoxical roles
1072 of mineral dust induced gene on cell proliferation and migration/invasion. PLoS One *9*,
1073 e87998.
1074 Zhu, J., and Thompson, C.B. (2019). Metabolic regulation of cell growth and proliferation. Nat
1075 Rev Mol Cell Biol *20*, 436-450.
1076